THE UNIVERSITY
OF ADELAIDE
AUSTRALIA

Guiding Light in Low-Index Media via Multilayer Waveguides

by

Kristopher J. Rowland

Supervisors:
Prof. Tanya M. Monro
Dr Shahraam Afshar Vahid

A thesis submitted in fulfillment of the
degree of Doctor of Philosophy

in the
Faculty of Sciences
School of Chemistry & Physics

December 2010

Chapter 2

Silica Air-Bragg Fibres

THIS chapter explores the guidance mechanisms of level-core air-guiding Bragg fibres whose cladding consists of alternating layers of a dielectric and air (or vacuum). This is done using both analytical and numerical techniques. Of particular interest is the existence and behaviour of higher-order bandgaps in such fibres—in particular, the potential to exploit their low-loss properties. This chapter is based on a publication compiled within the duration of research for this thesis: Kristopher J. Rowland, Shahraam Afshar V. and Tanya M. Monro, 'Novel Low-Loss Bandgaps in All-Silica Bragg Fibers', *Journal of Lightwave Technology*, Vol. 26, Issue 1, pp. 43-51 (8 pages in total), 2008 [Special Issue (post-deadline sessions—OFC 2007)]. In addition, the effects of connective struts and their placement between the (annular or polygonal) cladding rings on modal confinement loss spectra are also discussed.

Section 1.2.2 discussed the history and state of the art of Bragg fibres, but I will recap some important points here. The effectively one-dimensional nature of the Bragg fibre cladding is appealing in that the bandgaps available to the guided light can be greater in both bandwidth and number than those of a two-dimensional cladding. As discussed earlier, this follows from the general principle that bandgaps become more elusive as extra dimensions of periodicity are introduced into a structure [34]. The basic reason for this is that, as structure is introduced to more dimensions, light can 'fit' within the structure in a greater variety of ways; the more configurations light can adopt within a structure, the harder it is to find conditions where it is not supported. In other words, introducing greater dimensionality to the structure produces increased modal complexity which results in a greater coverage of the band spectrum, leaving few regions not covered by adjacent modes (*i.e.*, fewer bandgaps).

Even though they have a more complicated bandgap spectrum, hollow-core fibres with a 2-D cladding (like the honeycomb fibre, say) are appealing in that they can be fabricated from a single material. A single-material structure is freed from the restrictions imposed by structures like the conventional Bragg fibre which require more than one material to

construct, the greatest restriction being material compatibility. Air is chemically and thermally compatible with almost all practical fibre materials, while producing a large refractive index contrast at the same time. It would thus be ideal to have both a 1-D periodic cladding *and* a single material substrate: a Bragg fibre with an air-core and alternating dielectric and air layers: an *air-Bragg* fibre. Clearly the fabrication of a true air-Bragg fibre is impossible since the independent concentric dielectric rings would have no structural support. One must then resort to supporting the rings somehow. The most practical solution is to introduce connective struts between the layers.

In this vein, Vienne et al. [43] demonstrated a guiding hollow-core single-material Bragg fibre whose cross section consisted solely of silica and air. They showed that by using only three rings of silica layers connected by such struts, the novel fibre design can produce substantially improved light confinement than what can be achieved in conventional fibres such as the Bragg and honeycomb structures. For example, their so called 'OD90' fibre design was reported as having a low-loss hollow-core guidance bandwidth of over an octave (impossible via the other mentioned designs) with a nominal loss of ~ 1 dB/m using just three pairs of cladding layers. This behaviour is distinct from that of conventional (solid-cladding) Bragg fibres because the cladding and core share a common refractive index (air in this case: $n_{\text{air}} \approx 1$). When the core index has a value close to that of the lowest of the cladding layers, the supported core modes are able to intercept bandgaps that are significantly broader and more robust than those accessible by modes in a lower-index core. Analysis of this effect, and its exploitation, forms the basis of this chapter. Generalisation to cores with refractive indices below the lowest cladding index is dealt with in detail in Chapter 3.

Vienne et al. [43] modeled the confinement loss spectra of an idealised version of their OD90 fibre via an asymptotic transfer matrix method [176]. While the confinement loss values predicted were about 100 times lower than the total losses measured in the fabricated fibre, good agreement was achieved with respect to the predicted and observed transmission windows. This suggests that the dominant confinement mechanism is due to the 1-D periodicity of the cladding rings, with the connective struts perturbing the transmission spectrum by various means (increasing CL and introducing sharp loss features); a thorough understanding of the mechanisms responsible for how the connective struts alter the confinement loss spectrum is somewhat lacking. While there has been some significant progress towards explain the phenomenon [69–72], no convincing agreement between the modelling of the full fibre structure and experiment has been made. Section 2.7 analyses this topic further and presents some new results extending the findings of Refs. [69–72] to give more insight into these effects for a range of guided modes within various structures (with and without connective struts placed in various

arrangements between annular and polygonal rings). Nonetheless, as discussed, according to the experimental results of [43], it appears that the 1-D periodicity of the cladding plays a dominant role, so it is this behaviour analysed initially in § 2.4, generalising to the case of struts and polygonal rings in § 2.7.

The analysis of an idealised version of an air-Bragg fibre provides a vital foundation from which more thorough analyses can be based. Since the bandgap spectra of the idealised case apparently match well with transmission spectra of the fabricated fibre [43], it is fair to say the guidance is limited by confinement loss, *i.e.*, confinement loss is the dominant loss mechanism, at least for the current state of the art air-Bragg fibres. Confinement loss limited transmission has also been observed experimentally in conventional (solid-cladding) Bragg fibres for similar near-infrared (NIR) wavelengths [42]. It is thus important to find ways in which to minimise this loss. As will be shown in § 2.4, this can be achieved for idealised air-Bragg fibres by a simple global scaling of the cladding geometry to exploit higher-order bandgaps which naturally produce lower CL. Such global structure scaling is trivial to accomplish during the fibre drawing process, requiring only small changes in the fibre drawing parameters such as speed or temperature [177].

Other means of reducing confinement loss include the addition of more cladding rings or increasing the size of the core. The effect of adding rings to reduce confinement loss is well documented, as discussed in Chapter 1 above, but represents a significant increase in structural complexity. A natural alternative means to reduce confinement loss is to increase the size of the core, keeping the ring thicknesses constant. I will analyse this mechanism and demonstrate that, while effective, it requires impractical scaling of the core diameter in order to lower confinement losses to those achievable by exploiting a higher-order gap. Indeed, for the case considered, it is shown that the core radius would have to be about two orders of magnitude larger (at ~ 1 mm) than the core diameter required to achieve the same loss with the fundamental bandgap after a global structure scaling in order to shift the second-order gap to the working wavelength (producing a core radius of 24 μm). With a cladding pitch of the order of microns, such a large core would be extremely difficult to fabricate while maintaining the fibre details of the cladding. By maintaining a relatively small core, the cladding structure is easier to fabricate since the full extent of the structure is reduced. The following results thus point a way to reducing the confinement loss of full-structure air-Bragg fibres, where the nontrivial effects of the connecting struts are incorporated, without introducing additional or impractical structural requirements.

As discussed in Chapter 1, the reduction of losses within hollow-core waveguides is paramount for widening their applicability. The example of mid-infrared high-power delivery discussed earlier demonstrates how one must avoid even moderate waveguide

losses since, by absorbing a fraction of a large amount of power, they can have the potential to damage the waveguide structure (by melting it, for example). Reducing waveguide losses is also paramount for their many other applications such as sensing, nonlinear optics and particle manipulation, also discussed earlier.

Optimising confinement loss aside, this Chapter will also provide a commentary on the fundamental behaviour of guidance within this type of waveguide. In particular, it is noted how a rich bandgap spectrum exists for the 1-D cladding structure below the low-index light-line $\tilde{n} \leq n_0$. Unlike the typical bandgap spectra of 2-D cladding structures, such 1-D structures support bandgaps of substantial width and depth *below* (in the $\tilde{n}$ dimension) the regions where the gaps that intercept the $\tilde{n} = n_0$ light-line terminate. An in-depth analysis of this behaviour is given later in Chapter 3. It is also shown how the dispersion of the core modes is very well approximated by the equivalent modes supported in a dielectric tube of the same core size. This comparison is then used to explain the role of the addition of multiple cladding layers in affecting the guidance of light within the core.

2.1 Chapter Structure

Section 2.3 details the various modeling techniques used to analyse the idealised fibre and discuss points pertinent to the discussions of §§ 2.4 to 2.6. Section 2.4 analyses the dispersion and confinement loss properties of the considered fibre and its homogeneous-cladding analogue (a simple tube) and compares it to the bandgap and antiresonance characteristics of the cladding, elucidating some fundamental explanations for the behaviour of the air-Bragg fibre's guidance properties (such as features of the core mode confinement loss spectra). In particular, it is shown how there exists a second bandgap providing four orders of magnitude lower confinement loss than the fundamental and the reasons for this behaviour are discussed via the analyses just mentioned. Section 2.5 looks at the bandgap structure of the fibre cladding in greater detail, demonstrating a nontrivial bandgap topology uniquely accessible to such level-core Bragg fibres. Section 2.6 presents a way to exploit the second bandgap for potentially broadband air-core guidance with far lower confinement loss than that already observed [43]. Section 2.7 presents modal FEM analyses of the confinement loss spectra of a range of fibre cross-sectional structures based on an approximation to the structure of Vienne et al. [43] for various combinations of ring shapes and strut distributions; a discussion of the behaviour of the first three lowest order modes for each structure is presented. The details of the

modelling techniques used throughout (sans the FEM—detailed below, § 2.3.4) are covered in Appendix A, with the relevant sections referenced when appropriate. Concluding remarks are given in § 2.8.

2.2 Fibre Parameters

Here a level-core Bragg fibre geometry is considered: a circular core surrounded by concentric annular layers that alternate between two types; each layer type has a specific thicknesses and refractive index and the core has the same refractive index of the lowest of the cladding layers'. Taking r as the radial coordinate, the refractive index distribution of N layers is thus defined:

$$n(r) = \begin{cases} n_{\text{core}} = n_0 & \text{for} \quad 0 < r < r_0 \\ n_1 & \text{for} \quad r_0 < r < r_1 \\ n_0 & \text{for} \quad r_1 < r < r_2 \\ \vdots & \\ n_1 & \text{for} \quad r_{N-2} < r < r_{N-1} \\ n_0 & \text{for} \quad r_{N-1} < r < r_N \\ n_1 & \text{for} \quad r > r_N \end{cases}$$

where layers (excluding the core $0 < r < r_0$ and jacket $r > r_N$ regions) of the same refractive index n_i have the same thickness $t_i = r_i - r_{i-1}$. The core has radius $a = r_0$ and the outermost interface of the final cladding layer ($i = N$) is at $r = r_N$, the space beyond forming a high-index jacket[1]. More compactly:

$$n(r) = \begin{cases} n_{\text{core}} = n_0 & \text{for} \quad 0 < r < r_0 \\ n_i & \text{for} \quad r_{i-1} < r < r_i \quad \text{and} \quad i = 1 \rightarrow N \\ n_1 & \text{for} \quad r > r_N \end{cases}$$

where all even or odd numbered rings have the same refractive index n_i and thickness $t_i = r_i - r_{i-1}$, allowing one to define $n_i = \{n_1, n_0\}$ and $t_i = \{t_1, t_0\}$ $\forall$ $i = \{\text{odd}, \text{even}\}$. Thus, the cladding consists of $N/2$ unit cells (pairs of layers) each with a total width $\Lambda = t_1 + t_0$ called the *pitch* (the period of the concentric stack).

Fig. 2.1 is a schematic representation of a general level-core Bragg fibre where the refractive indices can generally take any value such that $n_1 > n_0 = n_{\text{core}} \geq 1$. The general level-core configuration is important for Chapter 3. Here, however, the special case

[1]This must be the case for the idealised air-Bragg fibre considered here as the jacket must consist of the substrate material. Other solid level-core Bragg fibres, however, often have a low-index jacket. The difference between the jacket types would likely only be a small confinement loss change, but it is an important point to consider if comparing the fibre types.

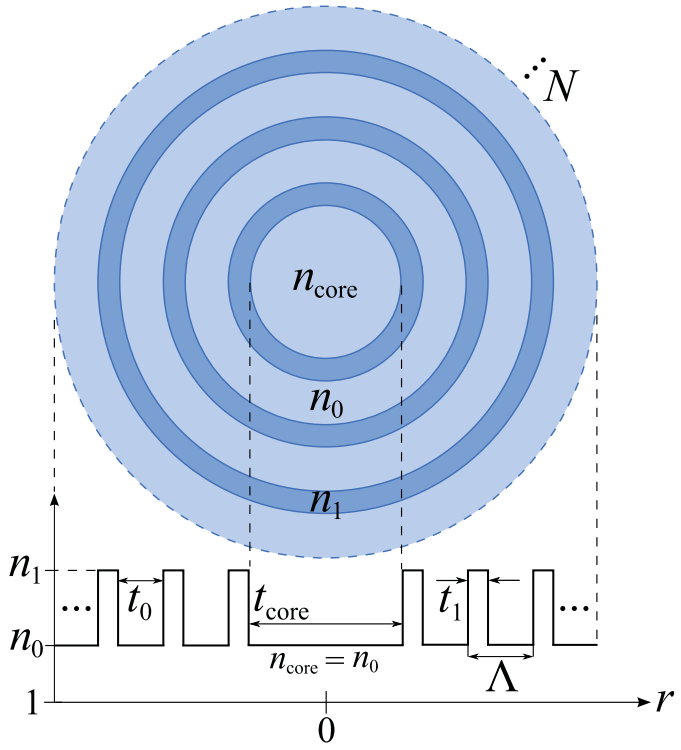

FIGURE 2.1: An arbitrary level-core Bragg fibre geometry. Refractive indices take any value such that $n_1 > n_0 = n_{\text{core}} \geq 1$. The calculations made here are for the idealised air-Bragg fibre case where $n_0 = 1$.

$n_{\text{core}} = n_0 = 1$ (vacuum/air) is considered: an idealised air-Bragg fibre. This configuration has five free parameters: the core radius $a = r_0 = t_{\text{core}}/2$, the two layer type thicknesses t_1 and t_0, the number of binary layer pairs N_{pairs}, and the refractive index of the high-index layer n_1. The main case considered here is the idealised silica air-Bragg fibre considered by Vienne et al. [43], namely: $a = 10$ μm, $t_1 = 0.37$ μm, $t_0 = 4.1$ μm, $N_{\text{pairs}} = 4$, and $n_1 = 1.45$ (approximately silica).

2.3 Background Theory

Here the theory used to analyse the problem at hand is presented. The reader should note that while the treatment here is intended to be brief, it is still somewhat detailed and has the potential to break the flow of the discussion. If desired, one can skip directly to § 2.4 to delve directly into the results and discussion, since the text refers back to the relevant background material when required. Nonetheless, the following theory components are put into context as they are discussed to maintain the work's flow.

Appendix A discusses all of the theory used in this Chapter. The relevant concepts and equations are highlighted here for ease of reference. As discussed in the introduction,

the content of Appendix A is not original to this thesis except where explicitly stated, and the relevant resources are referenced throughout. Note, however, that most of the theory covered in Appendix A has been re-derived such that many missing conceptual or mathematical steps in the source material have been included and expressed in a consistent nomenclature for completeness and ease of discussion here. Some modest novel results are also presented and highlighted as such within the Appendix.

Section 2.3.1 covers the modal guidance properties of a simple tube waveguide. Section § 2.3.2 discusses the Bloch mode bandgap properties of an infinite layer Bragg stack. Section 2.3.3 covers the theory of antiresonance (the ARROW model) for a single inclusion type, *i.e.*, for level-core multilayer waveguides. Section 2.3.4 discusses the modal guidance properties of multilayer cylindrical waveguides (Bragg fibres here), covering two modelling techniques: the transfer matrix method (semi-analytical) and the finite element method (fully numerical).

Two properties of guided light that will be often referred to here are the effective refractive index $\tilde{n}$ and confinement loss CL, also discussed in § 1.2.1. $\tilde{n}$ is defined directly from the longitudinal wavenumber (propagation constant) β of a guided wave: $\tilde{n} = \beta/k$ (§ 1.1). When solving electromagnetic waveguide problems like those used throughout this thesis (discussed in detail in Appendix A), one aims to find solutions to the full vectorial wave equation(s), *e.g.*, Eq. A.28. The problem can be cast as an eigen-problem whose eigen-solutions (*modes*) have specific field configurations associated with a discrete eigenvalue $\tilde{n}$. As an aside, given only the modal field configurations, the $\tilde{n}$ can actually be calculated directly from the integral relation Eq. A.26.

As discussed in § A.1.4 the real part of $\tilde{n}$, $\mathrm{Re}\{\tilde{n}\}$, contains information about the dispersion of the mode (essentially the phase it accumulates per unit length over various wavelengths) and the imaginary part $\mathrm{Im}(\tilde{n})$ corresponds to the attenuation of the mode. In the case of no material loss or scattering (from waveguide imperfections, say), this attenuation is entirely due to the confinement loss of the waveguide, pertaining purely to the guidance mechanism itself allowing leakage of the field out of the guidance region. Both of these effects are derived from the form of the modal fields in which a term of $e^{i\beta z}$ can be factored, *e.g.* Eq. A.21. As shown in Eq. A.25, this leads to a quantitative expression for the confinement loss related to the imaginary part of the propagation constant, or effective index, in units of dB as:

$$\mathrm{CL} = \frac{20}{\ln(10)}\mathrm{Im}\{\beta\} = \frac{20}{\ln(10)}k\,\mathrm{Im}\{\tilde{n}\}$$

Often when the effective index $\tilde{n}$ is referred to here without taking the real or imaginary parts, the real part is typically implied; context will indicate whether $\tilde{n} \in \mathbb{C}$ or $\mathbb{R}$.

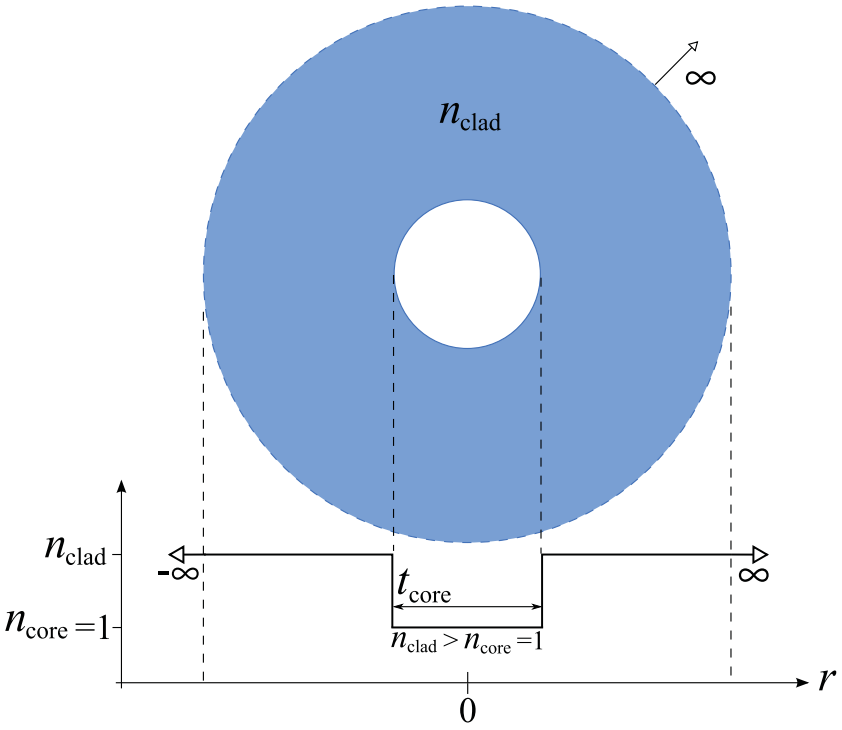

FIGURE 2.2: Schematic of a tube waveguide. The analysis here assumes an infinite the outer radius.

In general: if modal confinement loss is incorporated, $\tilde{n} \in \mathbb{C}$; if no confinement loss is considered (as is the case for planar waveguide, multilayer reflectance and Bloch bandgap analyses here), $\tilde{n} \in \mathbb{R}$.

2.3.1 Tube

It is useful to analyse the guidance behaviour of a simple hollow dielectric tube, such as that discussed in § 1.2. The dispersion and confinement loss properties of an idealised air-Bragg fibre will be compared to those of such a tube. It will be demonstrated how the mode conditions with respect to $\mathrm{Re}(\tilde{n})$, hence the dispersion properties, of the Bragg fibres considered agree closely with the modes of a simple tube (up to the effects of the Bragg cladding bandgaps).

Section A.4 describes the guidance of modes within cylindrical waveguides with a homogeneous cladding, a special case of which is a dielectric tube. The analysis itself is relatively involved, but can be deconstructed into a few fundamental steps. The parameters used to describe the tube are shown in the schematic representation of the structure in Fig. 2.2.

A basis of cylindrical wavefunctions satisfying Maxwell's equations are used to build solutions to an arbitrary cylindrically symmetric waveguide consisting of a homogeneous

core and cladding; Bessel functions of the first kind $J_l(r)$ are used for wavefunctions in the core in order to keep the field at the origin finite, while Hankel functions $H_l(r)$ are used for the cladding fields to ensure the appropriate out-going sinusoidal oscillatory behaviour of the fields as $r \to \infty$ (as expected for modes below cut-off—discussed in § A.4.1). Boundary conditions requiring the continuity of the electric field tangential to the core-cladding interface result in the formulation of a transfer matrix M relating the electric and magnetic fields within the core to those in the cladding. The system has eigen-solutions when the determinant of the transfer matrix equals zero: $\det(M)=0$. I explicitly demonstrate the expansion and simplification of this relatively complex determinant in Eq. A.171; something never shown in the literature, no doubt for brevity. Setting the determinant to zero and rearranging produces the *dispersion relation* or *characteristic equation* of the waveguide, Eq. A.173, which for dielectric media becomes Eq. A.174:

$$\left[\frac{J_l'(u)}{uJ_l(u)} + \frac{H_l^{(1)'}(v)}{vH_l^{(1)}(v)}\right]\left[n_0^2\frac{J_l'(u)}{uJ_l(u)} + n_1^2\frac{H_l^{(1)'}(v)}{vH_l^{(1)}(v)}\right] = l^2\frac{\beta^2}{k^2}\left(\frac{1}{u^2}+\frac{1}{v^2}\right)^2$$

where:

$$u = a\sqrt{k^2n_{\text{core}}^2 - \beta^2} = ak\sqrt{n_{\text{core}}^2 - \tilde{n}^2}$$
$$v = a\sqrt{k^2n_{\text{clad}}^2 - \beta^2} = ak\sqrt{n_{\text{clad}}^2 - \tilde{n}^2}$$

and $a = t_{\text{core}}/2$ is the core radius. This equation can be solved numerically to calculate the exact complex propagation constant $\beta \in \mathbb{C}$ for a dielectric tube, up to numerical precision. As mentioned above, the real part of $\tilde{n} = \beta/k$, $\text{Re}\{\tilde{n}\}$, contains information about the dispersion of the mode (essentially the phase it accumulates over various wavelengths) and the imaginary part $\text{Im}(\tilde{n})$ corresponds to the attenuation of the mode. In the absence of material loss and scattering (due to imperfections in the waveguide structure, say), the attenuation is entirely due to the confinement loss of the waveguide, pertaining purely to the guidance mechanism itself allowing leakage of the field out of the waveguide.

While the complex root-finding involved in solving this dispersion relation isn't exactly computationally intensive, a much more simple and analytic form of the solution $\tilde{n}$ can be found by considering the asymptotic form of Eq. A.174. Such analytic forms can give a powerful insight into the phenomena at hand and it is used here for that reason[2]. The analysis in § A.4.2 follows the treatment of Marcatilli and Schmeltzer [5]. By assuming a small wavelength relative to the core size and considering only low-order modes close to

[2]Indeed, much of the motivation for Chapter 3 is based on the fact that the theory there can be expressed in an analytic form such that it can elucidate similar physical insight.

the air-line ($\tilde{n} \approx n_0$), which is valid for all structures considered in this work, one finds that the dispersion relation can be simplified using the asymptotic forms of the Hankel functions and enforcing a perturbation analysis. One then finds that the solution to the characteristic equation can be approximated by (Eq. A.177):

$$\beta = \frac{2\pi}{\lambda}\left\{1 - \frac{1}{2}\left(\frac{u_{lm}\lambda}{2\pi a}\right)^2\right\} + i\left(\frac{u_{lm}}{2\pi}\right)^2 \frac{\lambda^2}{a^3}\nu_l,$$

$$\text{where} \quad \nu_l = \begin{cases} \frac{1}{\sqrt{n_{\text{clad}}^2 - 1}} & \text{for TE}_{0m} \\ \frac{n_{\text{clad}}^2}{\sqrt{n_{\text{clad}}^2 - 1}} & \text{for TM}_{0m} \\ \frac{n_{\text{clad}}^2 + 1}{2\sqrt{n_{\text{clad}}^2 - 1}} & \text{for HE}_{lm} \end{cases}$$

and u_{lm} is the m^{th} zero of the function J_{l-1}; approximate values of u_{lm} for the first few l and m indices are given in Table A.2.

$\text{Re}\{\tilde{n}\}$ and CL (Eq. A.25) can be evaluated from these expressions directly, namely:

$$\text{Re}\{\tilde{n}\} = 1 - \frac{1}{2}\left(\frac{u_{lm}\lambda}{2\pi a}\right)^2, \tag{2.1}$$

$$CL = \frac{20}{\ln(10)}\left(\frac{u_{lm}}{2\pi}\right)^2 \frac{\lambda^2}{a^3}\nu_l. \tag{2.2}$$

Note that the only dependence on refractive index is on n_{clad} in the imaginary loss term via ν_l, as may be expected from the ray picture's Fresnel reflection dependence. The real part has no dependence on the cladding index because, again considering the ray picture as described in § A.2, say, the mode condition is independent of the cladding index, where only the core index contributes to the accumulated round-trip phase of the ray (up to integer multiples of π on reflection).

The *transverse electric* (TE) and *transverse magnetic* (TM) modes referenced by the expression for ν_l refer to guided modes whose electric or magnetic fields (respectively) are transverse at all points to the core-cladding interface. The *hybrid* modes (termed HE, for 'hybrid electric', for historical reasons [178]) contain both electric and magnetic components normal to the interface [5]. The *mode indices* l and $m \in \mathbb{Z}^+$ are referred to as the azimuthal and radial quantum numbers, respectively, and determine how many local maxima a given mode has in each dimension; an excellent visual overview of the qualitative nature of each mode type is given in [5]. As demonstrated in § A, the transverse TE and TM modes require a null azimuthal quantum number (which in turn suppresses the z-component of the associated field—electric or magnetic), and so are always termed TE_{0m} or TM_{0m} (also see [146, 178, 179]). The hybrid HE modes

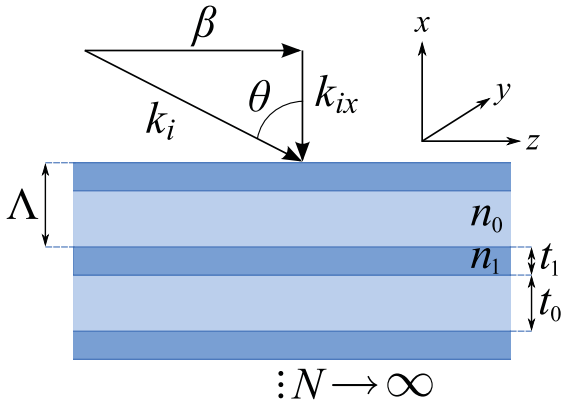

FIGURE 2.3: Schematic of an infinite Bragg stack. *Dark blue*: High-index layer with refractive index n_1 and thickness t_1. *Light blue*: Low-index layer with refractive index $n_0 < n_1$ and thickness t_0. The number of layers N is infinite. The vector diagram represents the decomposition of an incident ray's wavevector.

essentially represent all modes that aren't transverse and so have an azimuthal quantum number $l > 0$.

2.3.2 Infinite Periodic Multilayer Stack

As discussed in Chapter 1, the bandgap behaviour of the cladding of a Bragg fibre can typically be considered to be that of a planar 1-D Bragg stack [36, 37, 41, 42, 171, 180].

Section A.3.2 presents a Bloch wave analysis describing the propagation of light through infinite periodic multilayer planar structures. By restricting the structure to two layer types, the method describes propagation through an infinite Bragg stack. The technique is based upon a planar transfer matrix method (pTMM), discussed in detail in § A.3.1. There is an elegant way to describe the optical behaviour of an infinite multilayer stack, rather using the pTMM formalism for a finite number of layers N (producing $N/2$ pairs of layers), involving mathematical techniques exploited predominantly in solid-state physics. In fact, much of the following analysis (and § A.3.2) is isomorphic to the Kronig-Penney model used in solid-state physics to describe the energy levels of atomic lattices [181].

Consider a wave with wavevector $\mathbf{k}$, where $|\mathbf{k}| = k = \omega/c = 2\pi c/\lambda$ is the wavenumber and ω and λ are the wave's angular frequency and wavelength, respectively. The problem is simplified by, as depicted in Fig. 2.3, decomposing a supported wave's wavevector $\mathbf{k}_i$ into longitudinal (z-dimension) and transverse (x-dimension) components with amplitudes β and k_{ix}, respectively. The index i refers to the layer type the wave resides in and hence the background refractive index. The wavevector of a wave in the i^{th} layer is thus represented $\mathbf{k} = n_i k\hat{\mathbf{k}} = k_{iz}\hat{\mathbf{x}} + \beta\hat{\mathbf{z}}$. In the case of an infinite plane, the supported waves

could propagate with a y-z component in any direction, but the z-direction is chosen here to be consistent with the cylindrical coordinates chosen for the fibre case, as used throughout Appendix A.

The component with amplitude k_{ix} represents plane waves propagating normal to the interfaces of the stack. These plane waves will either be transmitted or reflected from each interface in the stack so that a the field of the wave in the i^{th} layer can be represented as a superposition of transmitted and reflected waves (Eq. A.102):

$$E_i = \left[A_i e^{-ik_{ix}(x-x_i)} + B_i e^{+ik_{ix}(x-x_i)}\right] e^{i(\omega t - \beta z)},$$

where A and B are the amplitudes of the transmitted and reflected waves; finding their values constitutes a solution to the problem.

The propagation of a wave through a unit cell (one pair of high- and low-index layers) of the infinite stack can be formulated as a transfer matrix problem. Taking the binary layer pair ($N = 2$) case of the general Eq. A.104, the field amplitudes can be related as:

$$\begin{pmatrix} A_{i-2} \\ B_{i-2} \end{pmatrix} = M \begin{pmatrix} A_i \\ B_i \end{pmatrix}.$$

The unit cell transfer matrix M can be decomposed into matrices describing the propagation across each interface and through each layer, labelled D and P respectively.

D is constructed from the Fresnel formulae (§ A.2.1.2) which describe reflection and transmission at an interface such that, for propagation from layer 'a' to layer 'b' (Eq. A.110):

$$D_{\text{ab}} = \frac{1}{T_{\text{ab}}} \begin{pmatrix} 1 & \Gamma_{\text{ab}} \\ \Gamma_{\text{ab}} & 1 \end{pmatrix},$$

where Γ is the *reflectivity* (Eqs. A.70 and A.72) of an interface and T is the *transmissivity* (Eqs. A.71 and A.73).

P is more simple, accounting for the phase accumulated while travelling through a layer. The transfer matrix for propagating through the i^{th} layer is (Eq. A.112):

$$P_i = \begin{pmatrix} e^{i\phi_i} & 0 \\ 0 & e^{-i\phi_i} \end{pmatrix},$$

where $\phi_i = k_{ix} t_i$ is the absolute value of the phase accumulated by a wave travelling in either direction.

The unit cell transfer matrix can thus be written (Eq. A.127):

$$M = D_{10}P_0D_{01}P_1,$$

where the subscripts 1 and 0 refer to the high- and low-index layers respectively.

The pTMM can be used to calculate the behaviour of waves within a *finite* number of layers, and is used this way in Chapter 3. In order to extend the analysis to the case of an infinite number of layers, one must employ the *Bloch-Floquet theorem* to relate the field amplitudes as demonstrated in detail in § A.3.2; Eq. A.122 states:

$$\begin{pmatrix} A_i \\ B_i \end{pmatrix} = e^{\pm iK\Lambda} \begin{pmatrix} A_{i-2} \\ B_{i-2} \end{pmatrix},$$

such that all components accumulate a phase of $K\Lambda$ after traversing the unit cell. The Bloch-Floquet theorem also states that the fields of such solutions, known as *Bloch waves*, will exhibit the same periodicity (Λ) as the lattice, as per Eq. A.120. K is known as the Bloch wavenumber and has a similar interpretation to the plane wave wavenumber k.

Since there are two ways to express the propagation across the unit cell, the problem can be cast as an eigenvalue equation (Eq. A.124):

$$M \begin{pmatrix} A_i \\ B_i \end{pmatrix} = e^{\mp iK\Lambda} \begin{pmatrix} A_i \\ B_i \end{pmatrix},$$

Solving this eigen-problem (see § A.3.2) is relatively involved, but ultimately produces eigenvalues $e^{\mp iK\Lambda}$ with a specific value related to the elements of M (Eq. A.152). The Bloch wavenumber can be found by adding together the two inverse eigenvalues, producing (Eq. A.153):

$$K(\tilde{n}, \omega) = \frac{1}{\Lambda} \cos^{-1} \left[\mathrm{Re}(M_{11}) \right],$$

where M_{11} is the first element of the unit cell transfer matrix (Eq. A.133).

Due to the Bloch wave x-dimension oscillatory term $e^{\pm iKx}$, as per Eq. A.120, the Bloch waves will be evanescent and hence decay into the structure when K is complex; note that the results I derive for Table A.1 are subtle but necessary and are not discussed in such detail in the literature. This condition happens when $|\mathrm{Re}(M_{11})| > 1$, making the cos factor in the solution for K complex. On the other hand, the waves will not be attenuated (ignoring material absorption, of course) when $|\mathrm{Re}(M_{11})| \leq 1$ and K is real, being permitted to propagate through the structure.

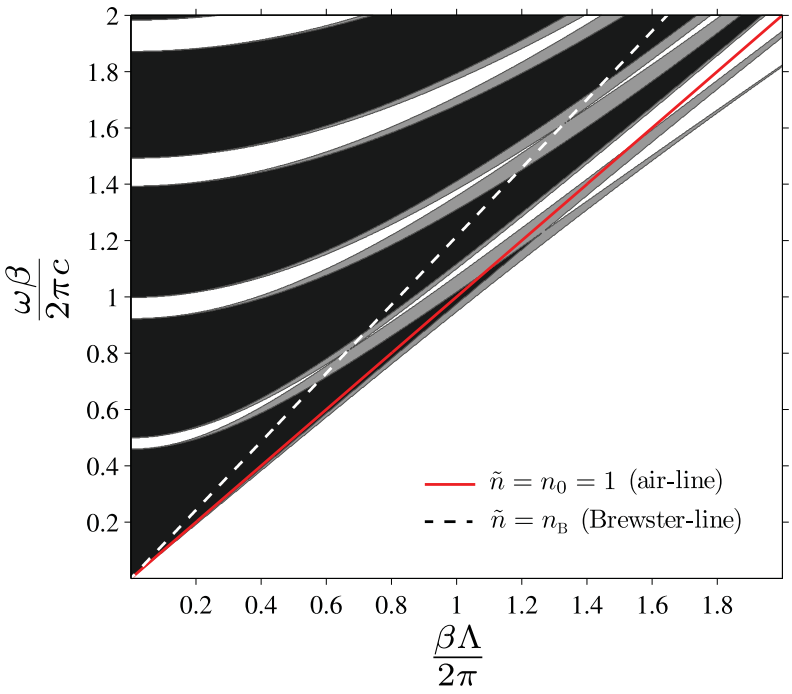

FIGURE 2.4: Bandgap map of an infinite 1-D approximation to the idealised air-Bragg fibre cladding. The Bloch wave existence condition $\mathrm{Re}(M_{11}) \leq 1$ map evaluated (grey regions—details given in the text) over unitless propagation constant $\beta\Lambda/2\pi$ and angular frequency $\omega\Lambda/2\pi$. *Solid red line*: Air-line $\beta = k = 2\pi/\lambda$. *White dashed line*: Light-line representing Brewster angle ray incidence ($\theta = \theta_B$); note that it coincides with the TM bandgap closure.

The regions of the $(\tilde{n}, \omega)$ plane corresponding to the condition $|\mathrm{Re}(M_{11})| \leq 1$ are said to constitute the *allowed bands* of the Bloch waves (their dispersion curves lying within these regions). The regions corresponding to $|\mathrm{Re}(M_{11})| > 1$ are said to constitute the Bloch wave *bandgaps* (regions where the Bloch waves are evanescent hence not permitted propagation). The band edges are thus defined by the Bloch mode dispersion curves satisfying $|\mathrm{Re}(M_{11})| = 1$.

These allowed band and bandgap regions can thus be calculated directly by simply evaluating the expression for the $K \in \{\mathbb{R}, \mathbb{C}\}$ conditions above for a range of $\tilde{n}$ and ω. It is useful to note that the $\mathrm{Re}(M_{11})$ factor can be expanded by using the expression for M_{11} in terms of the D and P transfer matrices, shown in Eq. A.133. I have derived a compact, polarisation invariant, explicit form of $\mathrm{Re}(M_{11})$ in Eq. A.154, where the phases are shown to be coupled as a sum or difference in the two terms:

$$\mathrm{Re}(M_{11}) = \frac{\cos(\phi_1 + \phi_2)}{T_{12}T_{21}} + \left(1 - \frac{1}{T_{12}T_{21}}\right)\cos(\phi_1 - \phi_2).$$

The TE and TM polarisation dependence has been relegated to Γ and T. Its evaluation requires only the input of the stack parameters n_1, n_0, t_1 and t_0, and the light wave

parameters $\tilde{n} = \beta/k$ and $k = \omega/c = 2\pi c/\lambda$.

Figure 2.4 shows the results of evaluating the Bloch wave existence condition $\mathrm{Re}(M_{11}) \leq 1$ map over unitless propagation constant $\beta\Lambda/2\pi$ and unitless angular frequency $\omega\Lambda/2\pi$ for the idealised air-Bragg fibre cladding considered here; these units are a common choice for representing bandgap maps, although a more appropriate choice for the work here will be demonstrated later. Note that the real part needn't explicitly be taken for β for the Bloch analysis since it is real by construction; the distinction between the real and imaginary parts must be made later, though, when leaky modes of the finite fibre structure are considered. The grey regions represent the allowed Bloch bands of the Bragg stack. Left of the air-line ($\beta < \omega/c$), the TE allowed band is the dark grey region and the TM allowed band is both the dark and light gray regions. The white region represents the TM bandgap and the white plus light gray regions represent the TE bandgap.

More correctly, in terms of set theory, the dark grey regions represent the *intersection* of the TE and TM bands and the light plus dark grey regions represent their *union*; this definition is only relevant when considering the bands also to the right of the air-line ($\beta > \omega/c$). The *complement* of either of these regions are thus the bandgaps of the associated TE or TM Bloch modes: those wave configurations disallowed from propagating in the cladding structure.

Note that to the left of the air-line (the region of most interest for this work), the TM band is always wider than the TE band so that *the TE bandgap is always wider than the TM bandgap*. This effect is entirely due to the Brewster phenomenon discussed in detail in § A.2.1.2. To explain this effect from a ray picture: since the reflectance of a TM ray is always lower than a TE ray, reaching precisely zero at the Brewster angle θ_B (Eq. A.86 and Fig. A.4), TM light is allowed through the periodic structure more efficiently than the TE light. The latter is thus reflected more at each interface which in turn manifests in the allowed TE Bloch bands being smaller than the TM bands (of course, the precise details require analysis of the pTMM itself (see § 3), but the concept is identical). Indeed, one finds that the TM gap closes up completely at the Brewster condition [63, 64, 172] $\beta = n_i k \sin(\theta_\mathrm{B})$ (white dashed line in Fig. 2.4), discussed in detail in § A.2.1.2. The Brewster closure effect becomes more important in Chapter 3, but the general reduction of the TM bandgap width is quite important for this chapter.

2.3.3 Resonance of a Single Layer—ARROW Model

Since the structure to be analysed is a level-core waveguide with a large core size and relatively large cladding pitch, the guidance mechanism can be approximated by an ARROW model as described for the level-core Bragg fibre and 2-D ARROW fibre discussed earlier in Chapter 1. The calculations presented within will demonstrate a quantitative agreement between the antiresonance and Bloch wave analyses in determining the high-loss regions of the waveguide.

Antiresonance models of low-index guidance state that the resonances of the cladding features *as they would exist if the feature were isolated from the surrounding structure* determine the wavelengths at which light is best coupled to the cladding and hence lost from the core [9, 99–102, 173]. As argued in the Introduction (*cf.* Fig. 1.7), for level-core structures this approximation is only accurate when the cladding features are sufficiently decoupled[3] (typically for a large pitch: $\Lambda \sim 10 \times \lambda$—as per § 1.2.3). In other words, in this regime, light is lost through the cladding most when it satisfies a mode condition within the cladding features. For level-core waveguides (the most studied structures for ARROW guidance), the appropriate cladding feature to consider is a high-index inclusion [99–102, 173].

In this case of a level-core Bragg fibre, one must consider the guided modes (resonances) of a high-index cladding layer embedded in an infinite homogeneous low-index background. As derived in § A.2.1.3, a single layer supports modes when a ray accumulates a round-trip phase of 2π. For the case of light originating from a low-index medium ($\tilde{n} \leq n_0$), the Goos-Hänchen phase shift is absent upon each reflection, the phase shift instead being only either 0 or π. Combining this with the phase accumulated by traversing the layer itself $k_{ix}t_i$, one can derive an analytic dispersion relation for all supported modes, Eq. A.99 for $i = 1$):

$$\tilde{n}_m = \left[n_1^2 - \left(\frac{m_1 \pi}{t_1 k} \right)^2 \right]^{\frac{1}{2}}, \quad m_1 \in \mathbb{N}$$

where m is the mode order and all other parameters have been defined above. TE and TM modes are degenerate due to the nature of the reflections for $\tilde{n} \leq n_0$. This expression can be rearranged (since it is analytic) into an expression for λ:

$$\lambda_m = \frac{2t_1}{m} \left[n_1^2 - \tilde{n}^2 \right]^{\frac{1}{2}}. \tag{2.3}$$

[3] Chapter 3 derives an accurate description of antiresonance for 1-D depressed-core waveguides, the SPARROW model, where decoupling doesn't seem as critical.

By setting $\tilde{n} = n_0$ (approximation for low-order modes in a level-core large core waveguide, corresponding to shallow ray incidence angles—see § A.2.1.3):

$$\lambda_m = \frac{2t_1}{m}\left[n_1^2 - n_0^2\right]^{\frac{1}{2}}. \tag{2.4}$$

These values of λ thus represent the resonances of the cladding layers as typically described in the literature [99–102].

For this $\tilde{n} = n_0$ formulation (Eq. 2.4), the antiresonance points are defined as the half-order resonances such that $m = \frac{1}{2}, \frac{3}{2}, \frac{5}{2}, \ldots$ [99–102, 173]. This is equivalent to taking the arithmetic mean of adjacent resonant wavenumbers $k_m = 2\pi/\lambda_m$:

$$k_m^{\text{antires.}} = \frac{k_i + k_{i-1}}{2} \tag{2.5}$$

such that the antiresonant wavelength of order m is $\lambda_m^{\text{antires.}} = 2\pi/k_m^{\text{antires.}}$. Being the mid-point between resonances in frequency space, these points represent the wavelengths at which the guided light is maximally *anti*-resonant with the cladding inclusions.

The case of $\tilde{n} \leq n_0$ is more complicated and its treatment is reserved for the theory I develop in Chapter 3.

2.3.4 Multilayer Cylindrical Waveguide

Two techniques are employed here in order to solve Maxwell's equations for the propagation constants and fields of guided modes within Bragg fibres: the *cylindrical transfer matrix method* and the *finite element method*.

Cylindrical Transfer Matrix Method Section A.5.1 presents the *cylindrical transfer matrix method* (cTMM) to generally describe the propagation of light within a cylindrical core defect enclosed by multiple concentric cylindrical layers. The method is closely based on the treatment of Yeh and Yariv [37]. By restricting the structure to two layer types and a depressed-index core, the method describes propagation within a Bragg fibre. Here the level-core structure of Fig. 2.1 is considered.

The solution technique is similar to that for the pTMM discussed above (details in § A.3.1) but where the solution waves are superpositions of incoming and outgoing cylindrical waves instead of plane waves and so must be composed of Bessel functions of the first (J_l) and second kind (Y_l) since they constitute a basis set of solutions for the cylindrical Helmholtz equation (Eq. A.46), the governing equation for longitudinally invariant waveguides with homogeneous subdomains, derived from Maxwell's equation.

The z-components of the electric and magnetic (auxiliary) fields about a given interface thus have form (Eq. A.182):

$$\{E_z, H_z\} = \begin{cases} [\{A_1, C_1\}J_l(k_{1x}r) + \{B_1, D_1\}Y_l(k_{1x}r)]\cos(l\theta + \{\psi_1, \phi_1\}) & r < \rho \\ [\{A_2, C_2\}J_l(k_{2x}r) + \{B_2, D_2\}Y_l(k_{2x}r)]\cos(l\theta + \{\psi_2, \phi_2\}) & r > \rho \end{cases},$$

where A_i and B_i are the relative field amplitudes to be solved for, ψ_i and ϕ_i are arbitrary azimuthal phase terms, and ρ is the radius of the particular layer interface (arbitrarily, this particular example has a type 1 layer for the small r side of the interface and a type 2 layer on the other side—the opposite will hold for an adjacent interface). As per standard cylindrical waveguide theory (see § A.1), the radial and azimuthal components of the fields E_r, E_θ, H_r and H_θ can be evaluated from the z-components alone, as per Eqs. A.40 to A.43.

As for the pTMM, a transfer matrix formulation can be established relating the fields in each layer to one another via the interface boundary conditions, this time for cylindrical waves and layers, though. The analysis is much more involved than for the planar case; again, a thorough treatment is given in § A.5.1. For the work in this chapter, only a finite number of layers are considered for this technique, so that the calculated core modes best represent the guidance properties of the idealised air-Bragg structure.

Ultimately, one can relate the field amplitudes from within the core to the outermost interface of the N-layer cladding via the simple matrix equation:

$$\begin{pmatrix} A_{N+1} \\ B_{N+1} \\ C_{N+1} \\ D_{N+1} \end{pmatrix} = M \begin{pmatrix} A_0 \\ B_0 \\ C_0 \\ D_0 \end{pmatrix},$$

where the, rather complicated, forms of the elements of the 4×4 matrices which constitute the total system transfer matrix M are given in Eqs. A.204. As for the tube solution above, one can then calculate $\det(M) = 0$ and solve for the propagation constant β (ensuring to enforce the physical condition of no incoming waves on the outermost layer [39]). For TE and TM modes, M reduces to a 2×2 matrix, simplifying (and hence speeding up) the numerical calculations required [39].

In general, for waveguides in which the core refractive index is lower than those of the cladding, an inherent modal confinement loss will exist, resulting in a complex propagation constant $\beta \in \mathbb{C}$ as discussed earlier. Indeed, it is precisely this behaviour that makes the cTMM so appealing: the ability to precisely calculate confinement loss

using a semi-analytical method. Such loss calculations are critical to the results discussed presently.

Finite Element Method The *finite element method* (FEM) is a purely numerical technique for solving partial differential equations that can be applied to waveguide analysis via the full vectorial wave equations Eq. A.28 and A.29, say—in particular, HC-MOFs [69, 182, 183]. Here the FEM is used to solve the Helmholtz wave equation Eq. A.46—the wave equation to which the full vectorial versions reduce to when considering homogeneous subdomains (as done here). The FEM is suited to waveguide modal analysis for practically any cross-sectional structure. A cost of this flexibility is increased complexity of the model and the increase in computational intensity for the numerical calculations required [183]. Because of this, for all FEM calculation within, the commercial FEM package COMSOL Multiphysics [182] is employed.

The fundamental premise of the FEM, as it's used here, is that each continuous domain of a structure is discretised into many smaller elements. The meshes generated for this work are based on triangular elements (quadratic Lagrange elements to be exact [182, 183]). An example of a mesh used to solve for core guided modes of the air-Bragg structures considered presently is shown in Fig. 2.5. This particular geometry is analysed later in § 2.7 whereas an idealised variant (in which the connective struts have been removed, leaving only concentric rings) is considered throughout the earlier sections.

The accuracy and precision of the numerical solution thus depends on the density of the mesh; the more information about the solution that can exist on the mesh, the closer the solution represents a 'true' mode. More correctly, the appropriate refinement of the mesh parameters (local element size and spatial distribution) will allow the model to *converge* to an accurate and precise solution. Generation of an appropriate mesh is quite nontrivial and typically relies on following some rules of thumb combined with trial and error. Such rules would be to make the mesh more fine (smaller elements, denser mesh) about regions of fine structural detail and about any other region where the solution will exhibit sharp field gradients. However, the greater the number of mesh elements, the greater the number of field discretisation values and hence the more information that must be calculated. A reasonably converged solution (with a sufficiently dense and appropriately distributed mesh) thus requires significant calculation power and memory resources.

The computer used for most FEM calculations within contained 24 GB of DDR2 RAM (with a 500 MHz bus speed) and an Intel Xeon eight-core processor architecture running at a 3 GHz clock speed with a 8 MB of total L2 cache. The total amount of RAM was rarely utilised since the bus speed produced the system's bottleneck; in order to iterate

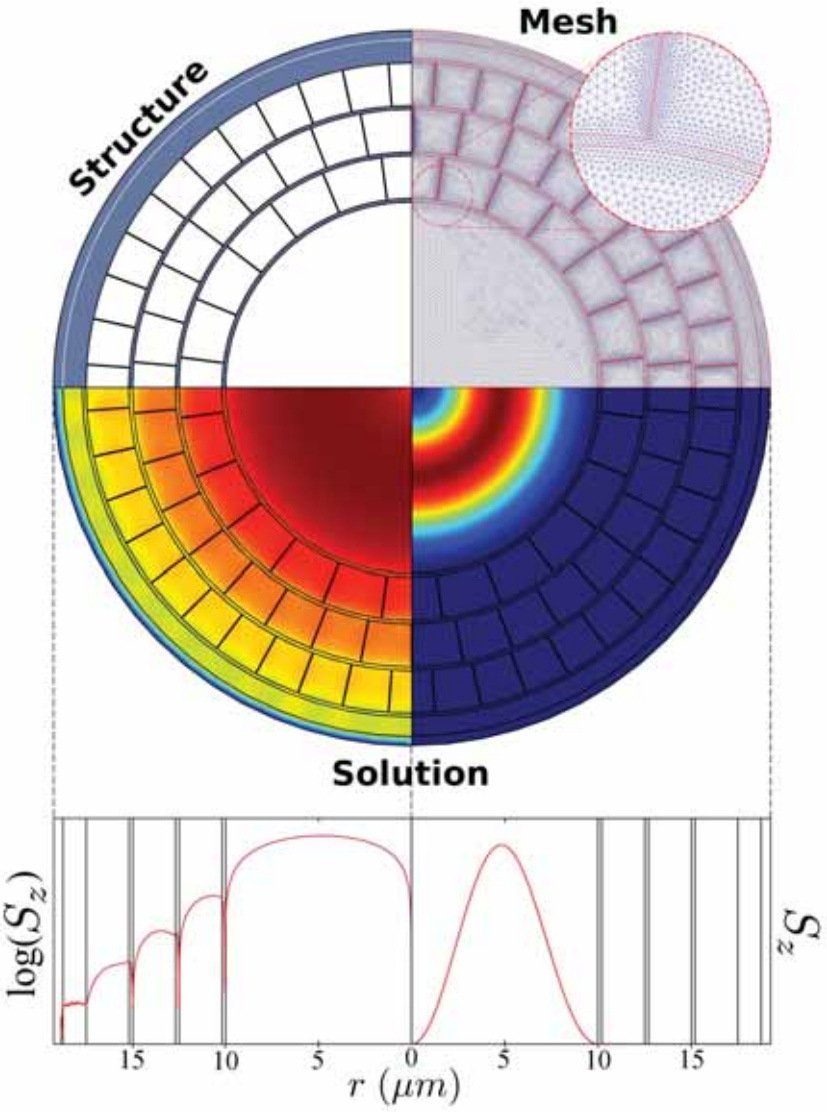

FIGURE 2.5: Geometry, mesh and solution example of a FEM model. *Top-left:* A quarter-plane representation of the geometry used to model the OD90 fibre of Vienne et al [43], using the simplified structure parameters of Refs. [71, 72], as described and used later in § 2.7. Dark regions: glass ($n_{\mathrm{Si}} \approx 1.45$). White regions: air. The thin annulus around the edge of the structure represents the PML. *Top-right:* distribution of the generated finite element mesh upon the truncated geometry. *Bottom:* an example of the fields of a numerical solution to the model [S_z and $\log(S_z)$ of the TE_{01} mode at $\lambda = 800$ nm, arbitrary units].

the FEM model thousands of times so as to calculate spectra of sufficient resolution, only about 8 GB of the RAM was accessed, bringing the calculation time per iteration down to approximately 10 to 15 minutes. Using one processor core, the 1000 iterations typically required for a reasonable spectral resolution thus took up to about 10 days to complete. Time was thus the predominant determining factor in the quality of the mesh used, hence the convergence of the solutions.

The geometries within consisting of only concentric rings (no struts or other features)

are typically converged over the considered full spectral range to a numerical error of less than $\pm 0.0001\%$ in $\mathrm{Re}(\beta)$ and less than $\pm 1\%$ in $\mathrm{Im}(\beta)$ (hence CL). For most other geometries, such as that of Fig. 2.5, calculated here can only be converged to within numerical error of less than $\pm 0.1\%$ in $\mathrm{Re}(\beta)$ and less than $\pm 100\%$ in $\mathrm{Im}(\beta)$. The latter may appear extreme, but since most interesting CL spectral features vary by orders of magnitude, this is not a terminal issue. Also, it is generally observed that the spectral features of a given solution maintain their relative magnitudes with respect to adjacent features, the numerical error (from altering the mesh density slightly, say) manifesting as a greater or lesser shift of the entire spectrum [$\mathrm{Re}\{\tilde{n}\}(\lambda)$ or $\mathrm{CL}(\lambda)$, say].

In defining the model, one must enforce the appropriate boundary conditions. Since all of the internal structure is dielectric, the usual continuity conditions are enforced for all interfaces internal to the solution domain (as used for the analytic and semi-analytic analyses in Appendix A). The outer boundaries, on the other hand, represent an artificial truncation of the geometry and hence must be treated appropriately. This is done in two ways.

First, all structures modelled via the FEM in this chapter (and Chapter 3) exhibit at least 4-fold symmetry (2 rotation and 1 mirror), meaning it belongs to the $C_{4,\nu}$ symmetry group [184]. Due to the symmetry of the constructed geometry, one can truncate the domain to a 1/4 azimuthal slice, as represented in Fig. 2.5. Owing to group theoretical arguments, this truncated domain can be used to simulate modes for which the boundary conditions support a given mode type [184, 185]. The modes of most interest here are the TE_{01}, TM_{01} and HE_{11}. For the case here, as per [184, 185], the TE_{01} mode is solved for by enforcing *perfect electric conducting* boundary conditions on the outermost boundaries of the truncated geometry: $\mathbf{E} \times \hat{\mathbf{n}} = 0$ at the boundaries ($\hat{\mathbf{n}}$ is the normal to a given boundary); this permits the characteristic azimuthal electric field polarisation of the TE_{01} mode. The some holds for the TM_{01} mode but under the so-called *perfect magnetic conducting* boundary condition: $\mathbf{H} \times \hat{\mathbf{n}} = 0$; this permits the characteristic radial electric field polarisation of the TM_{01} mode. The HE_{11} mode requires one of the boundaries cutting into the otherwise complete (full-plane) geometry to be perfect electric and one perfect magnetic; this permits the characteristic linear polarisation of the HE_{11} mode (linear in the direction of the perfect magnetic boundary). The polarisations just described should technically be termed *quasi*-azimuthal, -radial and -linear, owing to the vectorial nature of the system disrupting the field directions close to wavelength-scale features of large index contrast [186].

Beyond symmetry exploitation, the second requirement of domain truncation here is more vital to the ability to calculate confinement loss. Ideally one would model a domain of infinite extent since, in truncating the region beyond the waveguide structure with

perfect electric or magnetic boundary conditions, unphysical reflections are introduced into the model. These stray reflections must be suppressed in order to not only converge to a more physical solution, but in order to be able to calculate confinement loss. The latter is impossible using reflecting boundary conditions since no radiation is permitted to escape the calculation domain, hence there is a null loss value and a purely real propagation constant β [$\mathrm{Im}(\beta) = 0$]. One means of truncating the domain but maintaining a close to physical loss behaviour is to introduce an artificial absorbing region in place of the reflecting boundary. A *perfectly matched layer* (PML) is one such implementation of an absorbing domain commonly used for numerical electromagnetism [183, 187] and has been applied successfully to modal analysis of optical waveguides (*e.g.*, Refs. [69–72, 76, 78, 188, 189] (and in particular for the COMSOL package used here [182]). The PML itself is incorporated into the FEM calculation as an artificial inhomogeneous, anisotropic, absorbing medium which absorbs all incoming radiation regardless of field amplitude or orientation (up to numerical convergence). PMLs are thus a means of approximating a surrounding homogeneous medium of infinite extent. In practice, this requires a tensorial description of the artificial permittivity of the medium such that field lines approaching from any direction and of any amplitude are attenuated in a similar manner. The PML formulation used here is discussed in detail in [182, 187]. An example of a PML domain is shown in Fig. 2.5 as the outermost annulus surrounding the structure (the PML to solution domain interface is represented by the dashed white line, top-left).

By truncating the solution domain using the symmetry and absorbing PML techniques just described, the number of mesh elements required in order to discretise the geometry and solve for the appropriate eigenmodes is greatly reduced. Indeed, the calculation wouldn't be at all possible without the inclusion of an absorbing PML boundary domain (reducing the effectively infinite cladding region, requiring infinite memory to represent, to a finite one). The exploitation of the symmetry of the structure and supported modes allows a further reduction in the required number of mesh elements. Each vertex (node) and edge of a mesh element represents a set of field amplitudes and phases which, in aggregate across the entire mesh, form the characteristic discretised matrix of the waveguide system [183, 187]; the fewer mesh elements required, the more efficient the calculation in terms of required memory and computational power. Indeed, without truncating the domain to this extent, the calculation of the results presented below would have prohibitive, requiring greater computational resources than readily available.

2.4 Bragg Fibre Guidance and Low-Loss Bandgaps

The supported core modes of the idealised air-Bragg fibre structure as defined above in § 2.2 are analysed using a variety of techniques and comparisons. Section 2.4.1 presents calculations of the core modes of the idealised air-Bragg fibre ($\tilde{n}$ and CL spectra via the cTMM, § A.5.1 and FEM, § 2.3.4, methods) together with the bandgap calculations an infinite-layer approximation to the cladding structure (via the infinite pTMM, § 2.3.2). Section 2.4.2 details some phenomenological characteristics of the mode behaviour and explains it via considerations of the interaction of the core light with the cladding structure. The air-Bragg fibre modal behaviour is then compared with that of a homogeneous cladding analogue (a simple dielectric tube—theory in § 2.3.1) with various comparisons and contrasts made between the two waveguides in order to highlight common waveguidance features and mechanisms, highlighting how the simple form of the tube mode dispersion behaviour can be used to closely predict that of the Bragg fibre equivalent (up to band-edge effects). Section 2.4.4 discusses the relation of the dispersive and confinement loss properties of the Bragg fibre modes with the antiresonance (theory in § 2.3.3) behaviour of the cladding; comparisons between the bandgap and antiresonance mechanisms are discussed (preparing the introduction of the more general unification of bandgap and antiresonances for depressed-core waveguides in chapter 3). Section 2.4.5 then qualitatively discusses how all of these observations fit into practical scenarios, such as asymptotic single-modedness, the influence of structural deformations and the incorporation of connective cladding struts (the latter examined in detail later in § 2.7).

2.4.1 Core Mode and Bandgap Calculations

Only the TE_{01}, TM_{01}, and HE_{11} modes are calculated here as they represent the lowest-loss modes of their respective classes. While higher-order modes are by no means uninteresting or trivial, much of their behaviour can be inferred by first analysing their low-order counterparts. More importantly, it is well-known that the low-order modes of low-index guiding waveguides exhibit much lower loss than higher-order modes. This often leads to the waveguide being described as *effectively single-moded* or *asymptotically single-moded* [39, 43, 63, 64, 69, 171, 172]; the high-order modes are attenuated faster than the low-order ones such that in practice the transmitted light would consist predominantly of the lowest loss mode or modes. In the case of a Bragg fibre, the lowest loss mode is typically the TE_{01} mode [39, 43, 63, 64, 69, 171, 172], although it has been shown that under certain regimes this can change [49, 190]. Note, however, that the

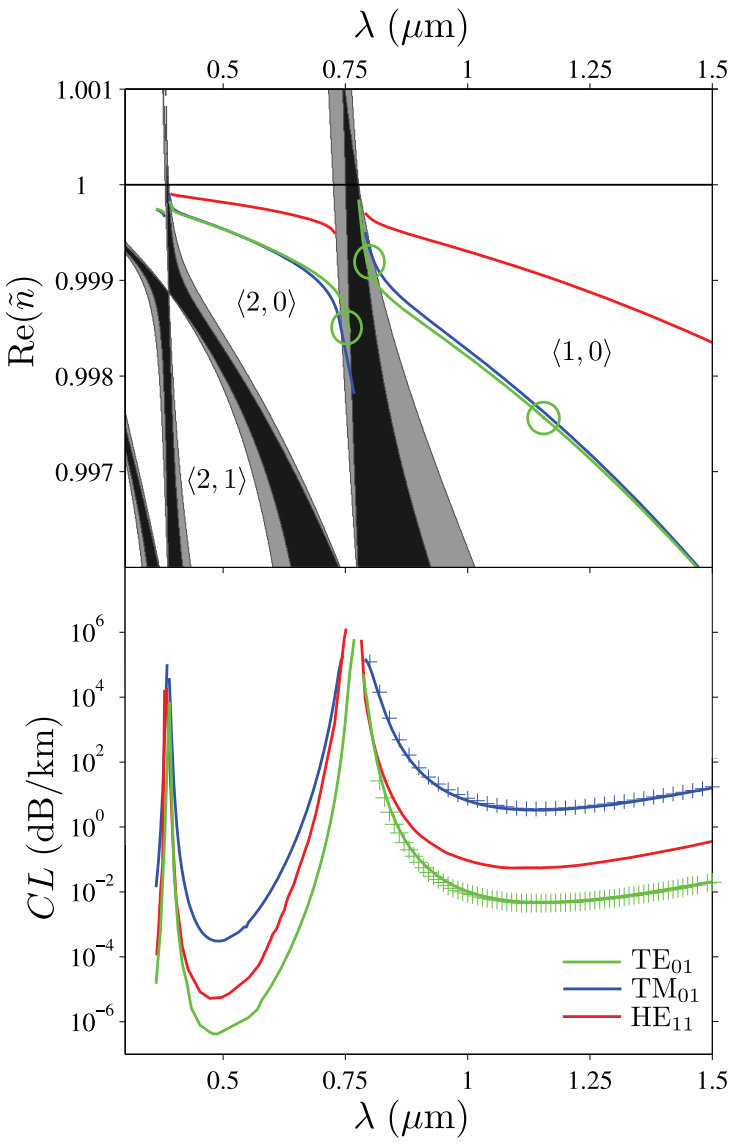

FIGURE 2.6: *Grey regions:* TE and TM Bloch bands of the equivalent 1-D infinite cladding stack; colour scheme explained in the text. TE bandgap nomenclature $\langle l, m\rangle$ is defined in § 3.7.1. *Black line:* Air-line ($\tilde{n} = n_0 = 1$). *Solid coloured lines:* Re$\{\tilde{n}\}$ (*top*) and CL (*bottom*) of the TE_{01}, TM_{01}, and HE_{11} modes of the idealised Bragg fibre found using the cTMM (for TE_{01} and TM_{01}) and FEM (for HE_{11}). *Crosses:* FEM calculations for CL of the TE_{01} and TM_{01} modes. *Green circles:* Sample points for evaluation of the fields in Fig. 2.7.

TE_{01} mode is not the lowest *order* mode since the HE_{11} has both the highest Re$\{\tilde{n}\}$ and only a single local maximum within the core region.

Dispersion curves Re$\{\tilde{n}(\lambda)\}$ and confinement loss spectra $CL(\lambda)$ of the first three low-order modes TE_{01}, TM_{01} and HE_{11} of the idealised air-Bragg fibre considered are shown in Fig. 2.6. The figure also shows the bandgaps associated with the cladding on the Re$\{\tilde{n}\}$ plot. It is important to note that both the bandgap maps and the CL spectra are considered together here. As discussed, the bandgap analysis is really an approximation

to the behaviour of the spatially finite waveguide, approximating the cladding as an infinite periodic planar structure, permitting the Bloch-Floquet analysis. Nonetheless, it is a very useful tool in explaining the behaviour of the core modes found via the more 'realistic' cTMM and FEM models. Both the Bloch wave and full structure core mode pictures offer valuable information and each have their benefits and drawbacks: the Bloch analysis is numerically cheap (evaluation of the semi-analytic expression $\mathrm{Re}(M_{11}) \lesseqgtr 1$) but is only an approximation to the spatially finite *cladding-mode* behaviour; the cTMM and FEM analyses give a comprehensive description of the *core mode* behaviour, including confinement loss, at the cost of numerical efficiency (§ 2.3.4).

Fig. 2.6 demonstrates these concepts: both cladding bandgaps and core-mode properties are represented on the same plot. The bandgap analysis is represented by the grey banded regions. The bandgap map is actually exactly the same as that shown in Fig. 2.4 but where the coordinates have been changed: $(\beta\Lambda/2\pi, \omega\Lambda/2\pi) \rightarrow (\lambda, \mathrm{Re}\{\tilde{n}\})$. The sloped light-lines $\beta \propto k$ thus become horizontal lines $\tilde{n} = \text{const.}$ in these new coordinates. The colour coordination of the bands is the same as for Fig. 2.4, but note that the region to the 'left' of the air line $\beta < \omega/c = k$ is now mapped to below the air line $\tilde{n} = \beta/k < 1$ and similarly for $\beta > \omega/c = k \rightarrow \tilde{n} = \beta/k > 1$, although the latter region is of little interest here as it can not be accessed by modes bound to the core of the Bragg fibre. This last point is a direct result of Corollary A.2 I derive in § A.2.1.2 where it is shown, via a ray picture, why modes guided in a low-index core are restricted to the region below the low-index light-line $\tilde{n} < n_0$ (*cf.* Eq. A.91).

The dispersion curves of the TE_{01}, TM_{01} and HE_{11} modes are overlayed on top of the band maps in Fig. 2.6, with the associated modal confinement loss $CL(\lambda)$ plotted below. $\mathrm{Re}(\tilde{n})$ and CL are calculated using the cTMM for TE_{01} and TM_{01} modes and the FEM for the HE_{11} mode. The TE bandgap nomenclature defined and used throughout this thesis—$\langle l, m \rangle$—is derived and defined in § 3.7.1. The green circles correspond to the points at which the field profiles were evaluated for Fig. 2.7.

All modelling considered here demonstrates an excellent agreement between the cTMM and FEM models, both in $\mathrm{Re}\{\tilde{n}\}$ and CL (Fig. 2.6). In the figure, where there are both cTMM and FEM results, the $\mathrm{Re}\{\tilde{n}\}$ values are indistinguishable between the two models (the HE_{11} mode was only calculated using the FEM for reasons of convenience). For the two modes that were calculated using both models (TE_{01} and TM_{01}), CL agrees to below 1%, resulting in the FEM data points (green and blue crosses, respectively) lying almost directly on top of the solid lines representing the cTMM results. Because of this excellent egreement between two disparate mode types (the TE_{01} and TM_{01} polarisation content and loss characteristics being distinct) one concludes that the two models are accurate representations of the system's solutions.

In comparison with the *asymptotic* cTMM results of [43] (where approximate asymptotic forms of Bessel functions are used in the analysis [40, 176, 191, 192]) for the same fibre structure, the non-asymptotic (and fully vectorial) cTMM and FEM results clearly produce a significantly lower CL ($\approx 20\times$). Since both the cTMM and FEM methods agree so well here, one can conclude that they are accurately converged and more appropriate models for quantitative modeling of CL in air-Bragg fibres; possibly due to the asymptotic field approximations upon which the asymptotic-TMM is based [176] breaking down for the level-core ($\tilde{n} \approx n_0$) regime.

2.4.2 Phenomenology

It is clear that by comparing the modes' dispersion and loss characteristics (Fig. 2.6) their confinement losses increase dramatically as the bandgap edges are approached. This behaviour is fundamental to the guidance mechanism of bandgap waveguides [2, 34, 41–43, 63, 64, 171, 172, 180] and is explained for the case here presently.

The modes' $\mathrm{Re}\{\tilde{n}\}$ lie relatively close to the light-line and generally continue to approach it as the wavelength decreases. This can be expected by analogy with the tube modes discussed above: Eq. 2.1 shows how $1 - \mathrm{Re}\{\tilde{n}\} \propto \lambda^2/a^3$. As $\lambda \to 0$, the modes thus approach the behaviour of a plane wave in vacuum as the core becomes relatively much larger than the wavelength. The fact that the cladding is structured in the Bragg fibre case is qualitatively of no consequence for this argument as the modes in each structure are confined predominantly to the core. The homogeneous-cladding and layered-cladding cases depart significantly in that the multiple reflections from the Bragg fibre's cladding layers reduce the confinement loss and also influence the dispersion and CL behaviour of the core modes as they approach the cladding bandgap edges. As will be shown in the next section (see Fig. 2.8), the modes closely follow the $\mathrm{Re}\{\tilde{n}(\lambda)\}$ trajectories of their homogeneous cladding (tube) counterparts until the bandgap edges are reached. Further comparisons with the analogous tube modes are made in § 2.4.3.

Indeed, the discontinuities for each mode, in both $\mathrm{Re}\{\tilde{n}\}$ and CL, correspond closely to the edges of the bandgaps. The TM_{01} mode exhibits slightly higher dispersion than the TE_{01} mode at the gap edges, which is expected from the Brewster phenomenon discussed earlier for the Bloch analysis (§§ 2.3.2 and A.3.2) which explain that the TM bandgap is always smaller than the TE gap (since the TM allowed bands are always envelop the TE bands).

This increase in confinement loss at the gap edges for all modes is qualitatively explained by noting that, as the bandgap edges are approached, light is increasingly allowed to propagate within the cladding. This effect is demonstrated by the behaviour of the

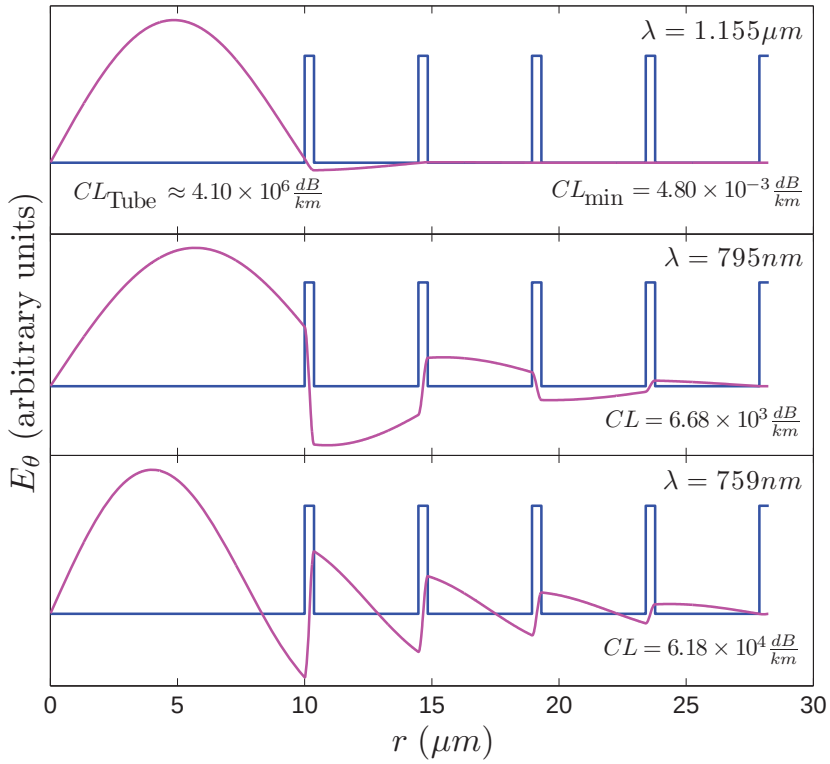

FIGURE 2.7: Azimuthal electric field component of the TE_{01} mode at the three wavelengths chosen from Fig. 2.6: 1.155 μm, the position of CL_{min} of the fundamental gap, where the light is most confined to the core; 795 μm, the low-λ band edge of the fundamental gap; and 759 μm, the high-λ band edge of the higher-order gap. The fields are overlayed on a radial slice of the refractive index profile. TE modes only have one nonzero electric field component: $E_\theta\hat{\theta}$. The field is azimuthally symmetric, so the field amplitude distribution has the familiar 'doughnut' shape with local polarisation everywhere in the direction of $\hat{\theta}$ (up to the sign of the field amplitude).

electric field profiles $E_\theta(r)$ of the TE_{01} mode shown in Fig. 2.7. Without the coherent reflection from the cladding that occurs for light deep within the bandgap, the mode's fields are able to penetrate further into the cladding structure, increasing the leakage of the field through the cladding and hence increasing the confinement loss[4].

The observation that modal confinement loss increases as bandgap edges are approached is a general one [63, 64]. This means that the modal confinement loss will increase regardless of the direction of approach to the bandgap edges, a point discussed in detail for the case of Bragg fibres by Argyros et al. [63]. Approach to the edges in the λ dimension is trivial, requiring only the wavelength to be changed. Approach in the $\text{Re}\{\tilde{n}\}$ dimension requires either the consideration of higher-order modes (which exhibit lower values of $\text{Re}\{\tilde{n}\}$ for a given λ) or, more importantly, the alteration of the core

[4]Note that it is possible for the evanescent fields of bound modes in small-core structures (such as optical nanowires) to increase in amplitude external to the waveguide structure without an increase in loss. This scenario is quite different, though, as such waveguides aren't inherently leaky and restrict guidance to $\tilde{n} > n_0$.

refractive index which necessarily alters the value of any supported mode's $\mathrm{Re}\{\tilde{n}\}$ since the core index represents the maximum asymptotic value for low-index guidance—*e.g.* §§ A.4 and A.2.1.2).

Note that reduction of n_{core} is not practical for the case here ($n_{\mathrm{core}} = n_0 = 1$) since n_{core} cannot be less than 1 for dielectric media, but the idea is perfectly sensible when $n_{1,0} > 1$ and is the case that forms the basis of the concepts of § 3. Confinement loss changes by traversing the $\mathrm{Re}\{\tilde{n}\}$ dimension are less trivial than those via the λ dimension since, in changing the order of a mode or the refractive index of the medium in which it is guided, the leakage loss will naturally change as well, even in the absence of a bandgap; this can be inferred directly from the CL behaviour of a tube in that $\mathrm{CL} \propto \nu_l$ which increases depends on the refractive index contrast. Nonetheless, as shown in [63], when bandgaps do exist, the band edges have a dominant influence on CL.

The increase in dispersion (slope of $\mathrm{Re}\{\tilde{n}\}$) of the modes near the band edges can be explained by noting that, as their field distribution increasingly overlaps with more of the cladding structure (Fig. 2.7), the influence of the various refractive index regions of the cladding structure causes $\mathrm{Re}\{\tilde{n}\}$ to rapidly depart from its trajectory as the field conforms to the cladding structure. This can be more qualitatively explained using the explicit expression for (the real part of) β as a spatial integral of the field components in Eq. A.26. With $\mathrm{Re}\{\tilde{n}\}$ being explicitly dependent on the field distributions within the various refractive index regions of the waveguide media, as the fields are increasingly permitted to penetrate the cladding structure their nontrivial overlap with the cladding features (Fig. 2.7) will directly alter the integral value of $\mathrm{Re}\{\tilde{n}\}$. In other words, as the field begins to overlap with the cladding, the phase conditions of the fields are influenced increasingly by the cladding layers; the modes' dispersion curves begin following the edges of the bandgaps since the layers themselves produce dispersion profiles closely following the cladding bands—*cf.* the photonic tight-binding model discussed in Chapter 1. In a sense, as the bandgap edges are approached and the modal fields are increasingly permitted to penetrate the cladding, the core modes begin to behave more as cladding modes, inasfar as their dispersive character is concerned.

With this in mind, note that the TE_{01} and TM_{01} modes' $\mathrm{Re}\{\tilde{n}\}$ lie almost exactly on top of each other, departing close to the band edges (Fig. 2.6). This quasi-degeneracy will be explained by comparison with the tube waveguide in § 2.4.3. Given that the modes are quasi-degenerate within the bandgap, the degeneracy splitting near the band edges can be explained with the argument of the last paragraph. The TE_{01} and TM_{01} modes will succumb to the bandgap behaviour of the TE or TM bands, respectively, since their fields at the layer interfaces satisfy transverse electric or transverse magnetic boundary conditions by definition. Since the TM gap is always smaller than the TE gap when

traversing the gap from the inside out, the TM_{01} mode will succumb to the dispersive effects of its band edges before the TE_{01} mode is effected by its more separated band edges. While the effect is subtle in this current case, it is an important observation, nonetheless. In fact, an extreme case can be seen in the works of [63, 64, 172] in which the TM type modes are suppressed altogether by designing the lowest order modes to be guided close to the Brewster condition where the TM gap closes up completely. This idea has the potential of permitting the low-loss guidance of only the TE_{01} mode, having suppressed most other mode types [63, 64, 172], including the HE modes which essentially contain a TM component.

Here it should be stressed that it is purely the properties of the guided modes themselves, *not* the cladding modes, that are responsible for the core mode behaviour between and close to the bandgap edges. While it is strictly true that the bandgaps are a representation of the guidance (or lack thereof) of cladding Bloch modes within an equivalent infinite cladding, the cladding modes exhibit no influence over the core-modes themselves, inasfar as their own field distributions and $\tilde{n}$ are concerned. As the core modes approach the bandgap edges, the tails of their fields succumb to the same influences of the cladding structure as enforced on the cladding mode fields and thus the core modes begin to behave *like* the cladding modes. This is essentially the behaviour embodied by the mode properties of Figs. 2.6 and 2.7 discussed above.

Cladding modes may also influence guidance by inter-modal coupling due to field overlap between the core and cladding modes. For the bandgap regime considered here, this is of little concern since the core mode has lowest loss within the bandgap region in which cladding modes are suppressed; not considering surface-modes [43, 70–73]. Core/-cladding inter-modal coupling does become feasible, however, for structures which guide via the Von Neumann Wigner phenomenon such as the Kagomé or square fibres discussed in Chapter 1. These structures permit cladding modes to co-exist within regions of low loss (antiresonance) of the core modes but, as discussed, it has been demonstrated how such coupling produces only a minor loss mechanism for the core modes as the core/cladding field overlap is very small for such large pitch structures [142, 145].

If approaching the bandgap edges increases the loss of a guided mode, a natural conclusion is that there will thus be a point between the bandgap edges where a guided mode has a locally minimal confinement loss $CL_{\min}$. This behaviour is explicitly observed in the CL curves of the modes shown in Fig. 2.6 in which the cladding bandgaps are seen to split the loss spectrum into two locally low-loss regions. The long-λ bandgap is the fundamental bandgap of the cladding. The shorter-λ bandgap will be referred to as the *second-order* gap. This nomenclature isn't general. The bandgap map of Fig. 2.6 shows how multiple simply-connected bandgap regions exist for the considered cladding

structure (not all gaps shown are labelled). The $\langle l, m\rangle$ labels used represent a general nomenclature for bandgaps of a 1-D layered structure which is derived in § 3.7.1. For now, only the two gaps just discussed are of interest, so the terms 'fundamental' (for $\langle 1, 0\rangle$) and 'second-order' (for $\langle 2, 0\rangle$) will suffice.

Fig. 2.6 shows how the calculated $CL_{\min}$ of all modes in the second-order gap are lower than their counterparts in the fundamental gap. Quantitatively, the CL of the TE_{01} mode in the fundamental gap has a minimum of $CL_{\min} = 4.80 \times 10^{-3}$ dB/km at $\lambda \approx$ 1155 nm. However, one finds that in the second gap the same mode has $CL_{\min} = 4.21 \times 10^{-7}$ dB/km at $\lambda \approx 480$ nm, which is four orders of magnitude lower than that of the fundamental gap. Note also that $CL_{\min}$ of *all* calculated modes decreases by this order from the fundamental to the second-order gap (Fig. 2.6).

The reason for the higher-order gap producing a lower loss lies in the fact that the modes' $\mathrm{Re}\{\tilde{n}\}$ lies closer to the n_{core}-light-line in the second gap than in the fundamental. The modes appear to approach an asymptote towards shorter wavelengths: $\mathrm{Re}\{\tilde{n}\} \to n_0$ as $\lambda \to 0$. This behaviour is explained soon in the context of the tube waveguide in § 2.4.3. This asymptotic behaviour can be used to give insight into the decrease in confinement loss in the higher-order gap. From a ray picture[5], $\tilde{n}_i = \beta_i/k = n_{\mathrm{i}} \sin\theta_i$ (Eq. A.90) implies[6] $\mathrm{Re}\{\tilde{n}\} \to n_0$ as the incidence angle approaches glancing $\theta \to \pi$, purely from the definition of β as the longitudinal wavenumber. The Fresnel formulae (Eqs. A.70 to A.73) imply that the reflectance of each interface is larger for rays of larger incidence angle (larger $\tilde{n}$). Thus, when the light is reflected coherently from the stack of layers—*i.e.*, at $CL_{\min}$ within a bandgap—the bandgap supporting modes with $\tilde{n}$ closer to the n_0-light-line will reflect light more efficiently since the reflectance from each interface is larger. Again, this a only a qualitative ray picture, but the concepts follow naturally from the plane-wave decomposition employed in the infinite stack pTMM analysis.

Also contributing to the reduction of loss as $\mathrm{Re}\{\tilde{n}\} \to n_0$ is the fact that the rays being reflected back into the core would experience fewer 'bounces' from the cladding per unit length than those with lower $\tilde{n}$. This is because the former rays would have a larger normal incidence angle θ (closer to glancing incidence) such that their trajectory would allow them to travel further before being reflected from the cladding again.

In the ray picture, then, there are thus two mechanisms at work acting to decrease $CL_{\min}$ in higher-order gaps: an increase in reflection efficiency for each interface (taking

[5]Of course, the ray picture is quantitatively insufficient for waveguides with guidance regions where diffraction effects become important, but it will suffice for the qualitative explanation of the large-core example here.

[6]Taking the real part of $\tilde{n}$ being redundant for this ray formulation as it is purely real by construction. One must still be careful and take the real part of the solution to the full wave equation solution, though, as it is naturally complex.

resonance/bandgap effects into consideration) and a reduction in the number of reflections per unit length. Both are the result of an increase in $\tilde{n}$ and hence an increase in normal incidence angle θ so that it approaches glancing incidence ($\theta = \pi$).

Ultimately, however, the interference effects of the light reflected from the multiple layers is dominant. This is seen in the fact that the second-order gap's CL calculated in [43] is higher than the fundamental's; the structure used was a variation of the one considered here: the layers had different thicknesses across the cross section. In this case, the interference effects for higher-order gaps (lower λ) become quite different for, say, the fundamental gap. This is discussed further in § 2.4.4.

2.4.3 Comparison with a Homogeneous Cladding

Fig. 2.8 is an adaptation of Fig. 2.6 in which the $\mathrm{Re}\{\tilde{n}(\lambda)\}$ and $CL(\lambda)$ for the analogous tube modes (§§ 2.3.1 and A.4.3) are shown together with the Bragg fibre modes.

Observe the behavior of $\mathrm{Re}\{\tilde{n}\}$ in Fig. 2.8: all calculated modes of the Bragg fibre lie on top of the trajectory of their tube analogues, deviating as they approach the band edges. Similarities between Bragg fibre modes and their tube analogues have already been observed in the context of surface modes [64], so its applicability here follows naturally. Thorough comparisons between Bragg fibres and hollow *metal* waveguides were performed by Johnson et al. [171]—*dielectric* tubes (as in Ref. [64]) are considered here. This deep connection between the two types of waveguide (homogeneous or layered cladding) is quite revealing.

As discussed in § 2.3.1, Eq. 2.1 implies that $\mathrm{Re}\{\tilde{n}\}$ for the tube is independent of the cladding properties; only λ and the core radius a are important as the ratio $(\lambda/a)^2$. In other words, only the core itself is responsible for tube modes' $\mathrm{Re}\{\tilde{n}\}$. This is also the case for the single layer waveguide discussed in § A.2.1.3 where the mode condition depends only upon the phase accumulated by a ray propagating through the core and the phase accumulated from reflection off of the interface. It was shown in detail in § A.2.1.2 how the reflection phase is equal to only 0 or π for light originating from a low-index medium. Recall that only low-index cores are of interest here; as discussed in § A.2, rays propagating in high-index cores succumb to total internal reflection which is coupled with the nontrivial Goos-Hänchen reflection phase shift which can take values from $0 \rightarrow \pi$ as a function of β and both the core and cladding indices. These arguments translate directly to the tube case so that one can see why the tube $\mathrm{Re}\{\tilde{n}\}$ would be independent of the cladding index (at least for the regime considered).

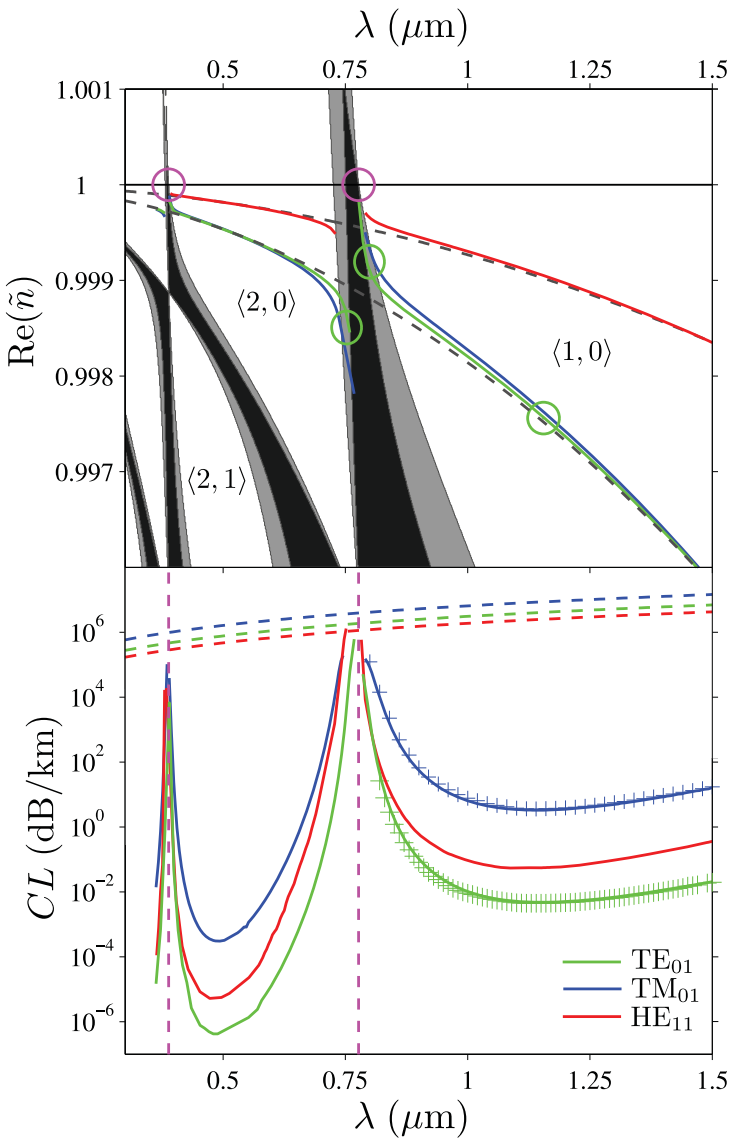

FIGURE 2.8: This figure is an adaptation of Fig. 2.6. *Grey regions:* TE and TM Bloch bands of the equivalent 1-D infinite cladding stack; colour scheme explained in the text. TE bandgap nomenclature $\langle l, m\rangle$ is defined in § 3.7.1. *Black line:* Air-line ($\tilde{n} = n_0 = 1$). *Solid coloured lines:* Re$\{\tilde{n}\}$ (*top*) and CL (*bottom*) of the TE_{01}, TM_{01}, and HE_{11} modes of the idealised Bragg fibre found using the cTMM (for TE_{01} and TM_{01}) and FEM (for HE_{11}). *Crosses:* FEM calculations for CL of the TE_{01} and TM_{01} modes. *Black dashed lines:* Re$\{\tilde{n}\}$ for the equivalent tube modes. *Coloured dashed curves:* CL for the equivalent tube modes. *Magenta circles and vertical dashed lines:* Cladding layer resonance wavelengths calculated from the 1-D ARROW model. *Green circles:* Sample points for evaluation of the fields in Fig. 2.7.

Since the mode trajectories of the tube agree so well with those of the Bragg fibre, one can infer that a similar mode condition holds for it as well. Indeed, according to Corollary A.2, a ray originating from a low index will not succumb to total reflection (and hence no Goos-Hänchen phase shift) at any subsequent interface. The accumulated phase from all reflections must then be an integer multiple of π. The phase from traversing the layers must also be incorporated, ultimately leading to the interference

effects accommodated for in the pTMM, cTMM and Bloch analyses. Thus, the Bragg fibre behaviour departs significantly from the tube as the modes reach the band edges, Fig. 2.8, as the fields leak into the cladding structure, Fig. 2.7. The tube and Bragg fibre modes thus agree so well within the bandgap since the Bragg fibre modes are suppressed within the cladding layers (Fig. 2.7) so that the phase accumulation within the layers has a negligible effect due to the field strength being so low there; the phase accumulation in the core is dominant.

These comparisons between HC-MOF tube guidance are closely related to the experimental and theoretical work of Issa et al. [95] in which the core, not the surrounding microstructure, was found to be the dominant guidance mechanism of a polymer bandgap fibre (although it was discovered that the disorder in the fabricated cladding destroyed any measurable bandgap behavior, actually reducing the waveguide to essentially the behaviour of a tube).

This dominance of the core in the guidance of both the tube *and* Bragg fibre thus explains why the Bragg fibre mode trajectories approach an asymptote towards short wavelengths: $\mathrm{Re}\{\tilde{n}\} \to n_0$ as $\lambda \to 0$. From the tube dispersion relation Eq. 2.1 one sees this behaviour directly since $1 - \mathrm{Re}\{\tilde{n}\} \propto \lambda^2/a^2$ so the same general trend should be followed by the Bragg fibre, at least within the bandgaps where light is restricted mostly to the core. This is also seen in the planar waveguide case where, from Eq. A.99, precisely the same proportionality holds: $1-\mathrm{Re}\{\tilde{n}\} \propto \lambda^2/t^2$. Here, this behaviour comes directly from the phase accumulated by a wave from propagation through the layer's core (up to terms of π due to reflection) as demonstrated in § A.2.1.3, and the equivalent principle holds for the tube and thus Bragg cases as argued.

Fig. 2.8 also compares the CL of the Bragg fibre and equivalent tube, showing that, within the bandgaps, the coherent reflection from the Bragg cladding reduces the CL significantly. The addition of the Bragg layers reduces the $CL = 4.10 \times 10^6$ dB/km of the tube by 9 orders of magnitude down to $CL_{\mathrm{min}} = 4.80 \times 10^{-3}$ dB/km at $\lambda = 1155$ nm within the fundamental gap. The effect is even more pronounced for the second-order gap where $CL =$ of the tube is reduced by 13 orders of magnitude to $CL_{\mathrm{min}} = 4.21 \times 10^{-7}$ dB/km at $\lambda = 480$ nm. It should be noted that the structure considered only has 4 cladding layer pairs; the reduction in confinement loss for level-core 2-d HC-MOFs is typically about 10 dB per additional ring [76]. This idealised air-Bragg structure reduces loss, on average, by more than 100 dB per unit cell for the fundamental gap and over 1000 dB per unit cell for the second-order gap, again demonstrating how the wide bandgaps produced by the air-Bragg structure are superior to many other geometries. This was seen explicitly in the experimental results of Vienne et al. [43] in that the low-loss bandwidth spanned over an octave, even though the

spectrum was interrupted by the effects of the supporting struts [70–73] and other likely loss mechanisms.

The arguments given above regarding modes lying close to the light-line having lowest loss are verified explicitly for the tube case. CL curves of the tube clearly monotonically decrease of decreasing wavelength, Fig. 2.8. This is due to the fact that $CL \propto \lambda^2$ (Eq. 2.2). As discussed above, from a ray picture $\tilde{n}$ approaching the light-line is equivalent to bound rays approach glancing incidence, thus confinement loss is reduced as the Fresnel reflectance is increased (Fig. A.4) as discussed for the layered case earlier.

2.4.4 Antiresonance Approximation

Figure 2.8 also shows the resonance wavelengths of a planar approximation to a high-index cladding layer in isolation. This represents an ARROW model as described above (§ 2.3.3 and further in Chapter 3). The Bloch bands themselves are shown to be relatively thin (in the λ dimension), which is due to the relatively large cladding pitch ($\Lambda = 4.1$ μm versus, say, the first Bloch bands on the light-line at $\lambda \approx 750$ nm—Fig. 2.8) beginning to induce a decoupling effect between the cladding rings, as discussed in Chapter 1: the interaction between the layers is reduced, reducing the splitting of the coupled waveguide degeneracy [9, 36, 104, 153]. This is also the regime in which the ARROW model may be accurately applied; each layer is approximately decoupled from the others so the modes (resonances) of the layers (in isolation) determine the high-loss regions of the core modes (discussed at length in Chapter 1). ARROW models for level-core waveguides with a large core size typically only calculate the cladding resonances at cut-off [99–102, 173]; that is, only the mode conditions at $n_{\text{core}} = n_0$ are calculated since the bound modes reach cut-off (cease to be bound) at this point (called the low-index *light-line*—the propagation constant of a plane wave travelling through a homogeneous region of the same refractive index). The generalised antiresonance model presented in Chapter 3 actually extends the consideration of resonances to below the cut-off condition, hence accurately describing modes that exist significantly below the light-line.

The first two cut-off resonance wavelength points superimposed on the bandgap map in Fig. 2.8 are: $\lambda_1 = 777$ nm and $\lambda_2 = 388.5$ nm. They clearly coincide with the first and second order Bloch bands (the short-λ edges of the first and second order bandgaps), respectively, as expected from the ARROW model and the tight-binding model of band formation [9, 36, 104, 153]. Of interest is that the resonances reside precisely on the edge of the Bloch bands, not in them as appears common for 2-D cladding waveguides [9, 104]; this phenomenon warrants further investigation as to the precise relationship between the Bloch waves of an infinite stack and the modes of a single layer (one might suggest

that the answer is related to the tight-binding Bloch wave phenomenon discussed in Chapter 1).

These resonance points are also overlayed as vertical lines on top of the confinement loss curves in Fig. 2.8. There is a very close agreement between the high-loss regions of all calculated modes and the resonance points, as expected from the ARROW model. The antiresonance points (the mid-points in frequency space between adjacent resonances) are $\lambda_1^{\text{antires.}} = 518$ nm and $\lambda_2^{\text{antires.}} = 1036$ nm. These coincide reasonably well with the $CL_{\min}$ points in the fundamental and second-order gap, which occur at $\lambda = 1155$ nm and $\lambda = 480$ nm, respectively, as discussed. These $CL_{\min}$ are thus 7.73% and 11.9% (respectively) away from the antiresonance points normalised to the bandwidth between adjacent resonances (all in frequency). The reason for the discrepancy is that, as discussed, on the air-line the Bloch band edges extend into the region between the resonances; *i.e.*, the bandgaps on the air-line are somewhat smaller than the distance between the associated mode cut-off points. This is an artifact of residual coupling between the layers broadening the Bloch bands. This has the effect of shifting the position of $CL_{\min}$ away from the antiresonance point in each gap.

Were the core modes to exist at lower $\tilde{n}$, they would intercept ever more nontrivial band edges which do not align with the cut-off resonances even qualitatively. This observation forms the motivation of the analysis of Chapter 3 and the subsequent invention of the SPARROW model developed within it.

2.4.5 Practical Considerations

As mentioned above, it is often quoted that Bragg fibres are effectively, or asymptotically, single-moded [39, 43, 63, 64, 69, 171, 172], since the TE_{01} mode typically has a substantially lower confinement loss than all other supported modes. This case is obviously no exception as per Fig. 2.8. The assumption of differentiation of modes purely due to a splitting of confinement loss values may be somewhat optimistic, though. The difference between the propagation constants β of two modes determines the extent of coupling between them due to various effects (such as fibre deformations like surface roughness or microbending) [146]. Since the $\text{Re}\{\tilde{n}(\lambda)\}$ of the quasi-degenerate TE_{01} and TM_{01} and modes lie very close to one another within all gaps (Fig. 2.8) the considered fibre would only be asymptotically single-moded when inter-mode coupling is minimised. By considering the tube equivalents of the fibre modes (explained in §§ A.4 and A.4.3), it can easily be shown that only 8 modes lie within the higher order bandgap and have considerably separated $\text{Re}\{\tilde{n}\}$ compared to the separation of the quasi-degenerate modes (note that the HE_{21} mode is also quasi-degenerate with the TE_{01} and TM_{01} modes,

§ A.4). It is thus likely that, in the presence of inter-mode coupling (due to scattering, say), the four modes with lowest total loss per unit length would be the quasi-degenerate TE_{01},TM_{01} and HE_{21} modes (linked via inter-mode coupling) and the HE_{11} mode (since its CL typically has values between the TE_{01} and TM_{01} modes, as discussed). Even in the face of this probable multi-modedness, it is clear that the higher order bandgap may be exploited to produce modes of overall lower CL, Fig. 2.8. In this way, low-loss (albeit potentially multi-mode) propagation can be achieved. This is explored further in § 2.6.

It is interesting to note that Vienne et al. [43] actually calculate the higher order gap CL for their structure (very similar to that considered here) but where the cladding layers have different thicknesses as exhibited by their fabricated OD90 fibre. Since the cladding layers aren't periodic in that case, one can't use the bandgap analysis used here. In their work, the CL values of the modes in the second-order gap are actually shown to be higher than those of the fundamental gap. This effect, however, is almost certainly due to the aperiodicity of the cladding layers. In antiresonance terms, as the cladding layers deviate in thickness, their resonances are shifted along the spectrum: thinner rings produce resonances at shorter λ (obvious once scale-invariance is considered and seen directly in the form of λ_m in Eq. 2.4). With rings of differing thicknesses, then, the resonances from one will fall between those of an adjacent ring. This has the effect of interrupting higher-order gaps more than low-order ones. To see this, consider Fig. 2.8: by decreasing the thickness of a ring, the resonance of the first band would be shifted such that it sits within the original second-order gap; there would be no equivalent disruption of the fundamental gap. This reduction in anti-resonance bandwidth explains why the modes calculated in the second-order gap in [43] have a higher loss than those in the fundamental. For this reason, periodicity (or at least equal high-index ring thickness) is more important for higher-order gaps than for the fundamental gaps.

In practice, the addition of supporting struts between the cladding layers, as in [43], would alter the CL of all bandgaps by two effects: an increase in 'tunnelling' through the cladding and the introduction of nontrivial resonance effects such as coupling to surface modes. Surface modes have been studied extensively in conventional hollow-core silica bandgap fibres [81, 126, 128, 193] as discussed in Chapter 1. Calculations from recent work have shown that surface modes exist in single-material Bragg fibre structures, introducing a complicated structure to the CL spectrum by coupling with the core modes [70–73]. However, as discussed in Chapter 1, such modelling is in rather poor agreement with experimental results [43] in that the calculated low-loss modal CL spectra do not correspond to the experimentally measured transmission spectra, indicating that surface modes likely aren't the only important phenomena introduced by the addition of struts. Indeed, the influence of tunnelling and other, non-surface-mode, cladding effects due to the introduction of struts is still poorly understood. However, in light of

much recent work on novel hollow-core microstructured fibres based on square [159, 160] and Kagomé [9, 141–145] cladding geometries, it seems that the understanding of such effects may be related to a Von-Neumann Wigner phenomenon [9, 142, 145, 150–152], in which modes may be guided in the core amidst even a continuum of cladding modes [142, 144, 145]. Nonetheless, as is shown in §§ 2.7 and 5.5, the radial 1-D structure plays a pivotal role in the guidance mechanism.

Since the CL spectrum is determined by a combination of the radial periodicity and other potential strut-induced phenomena, only after the idealised 1-D case is understood can the behavior of a full, strut-laden, structure be appreciated. Further, the conclusions which may be drawn from the semi-analytical treatment given here would be very difficult to deduce from a full-structure model alone, precisely because of the increased complexity. Thus, the main focus here is to analyse the idealised bandgap behaviour which may be used to provide the groundwork for analysis of fabricable geometries.

2.5 Analysis of Bandgaps

To investigate the behavior of the second bandgap further, the structure of the cladding bandgaps is now considered in more detail. Fig. 2.4 shows the Bragg cladding bandgap maps evaluated over unitless propagation constant and angular frequency $(\frac{\beta\Lambda}{2\pi}, \frac{\omega\Lambda}{2\pi c})$. This is the usual representation of Bragg stack bandgaps used in most literature.

This first representation shows where air-core modes would lie in the first bandgap since the actual dispersion curves, Fig. 2.8, of the low order modes are almost indistinguishable from the light-line in this representation. From this one sees that this level-core fibre has dispersion properties quite dissimilar to depressed-core Bragg geometries where $n_{\text{core}} < \{n_1, n_0\}$ [10, 35–47, 63, 171, 172]. Instead of the core's light-line intersecting the bandgaps somewhere in the middle, here it lies close to the region where the bandgaps terminate. This is entirely due to the fact that here $n_{\text{core}} = n_0$. Fig. 2.4 clearly shows how the $(\frac{\beta\Lambda}{2\pi}, \frac{\omega\Lambda}{2\pi c})$ representation makes it difficult to determine the interaction of the light-line with the bandgaps for fibres satisfying this condition since the band features close to the light-line seem to approach it asymptotically. In order to reveal this hidden detail, one must find a way of re-scaling the band map.

By transforming the band diagram to new coordinates $(\Lambda/\lambda, \text{Re}\{\tilde{n}\})$, as in Fig. 2.9, the detail close to the air-line in Fig. 2.4 is exposed. Immediately one notices how the bandgap structure in the region close the the air-line is very different to most of the the gaps shown in Fig. 2.4. Represented in these coordinates, the bandgaps clearly have a far richer structure than one would have previously thought.

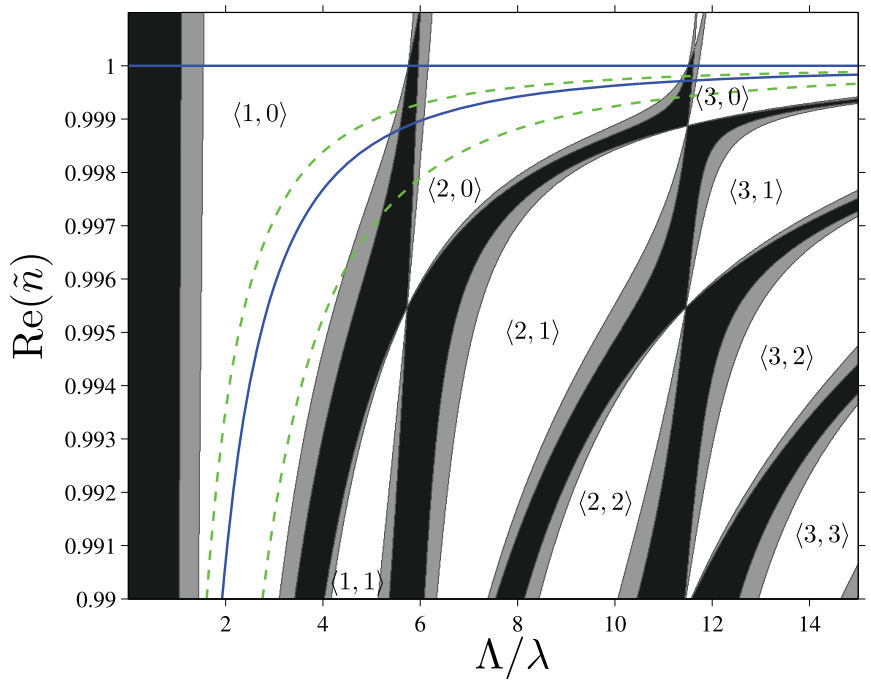

FIGURE 2.9: The same map as Fig. 2.4 recast in unitless, scale-invariant, frequency Λ/λ and real effective index $\mathrm{Re}\{\tilde{n}\}$ coordinates. The color scheme for the bandgap maps has been retained and the TE bandgaps are again labeled according to the system discussed in § 3. *Blue line:* air-line. *Blue curve:* The mode trajectory of the $l = 0$, $m = 1$, modes of an $a = 10$ μm radius tube (TE_{01},TM_{01} and HE_{21} tube modes are degenerate in $\mathrm{Re}\{\tilde{n}\}$). *Dashed green curves*: Same as the blue curve but for $a = 12$ μm (above) and $a = 7$ μm (below).

The higher order bandgaps of the Bragg stack clearly aren't simply connected (Fig. 2.9), as may be assumed from the original representation (Fig. 2.4). The first order gap *is* simply connected $\forall\ 0 \leq \tilde{n} \leq 1$ (at least for these fibre parameters[7]), but all higher order gaps close at points within $\tilde{n} = 0 \rightarrow 1$ and open up again as new gaps. Note that this gap closure is wholly *unrelated* to the Brewster phenomenon [indeed, the Brewster condition corresponds to a constant value $\tilde{n} = \tilde{n}_B = n_i \sin(\theta_B)$, § A.2.1.2, far below the plotted domain of Fig. 2.9].

A general nomenclature is derived for these discrete bandgaps in § 3.7.1, where it is shown that each TE gap can be referenced by a unique integer pair[8] $\langle l, m\rangle$. Here it will suffice to observe that l typically increases with increasing frequency (Λ/λ) and m increases with decreasing $\tilde{n}$. More specifically, at each TE gap closure point, the corresponding gap on the high-frequency side will have indices $\langle l+1, m-1\rangle$ with respect to the indices $\langle l, m\rangle$ of the corresponding gap on the low-frequency side of the closure point, *i.e.*, traversing

[7] See § 3 for a general description.

[8] The $\langle l, m\rangle$ nomenclature of § 3.7.1 is truly general, applicable to any Bragg fibre configuration (not just air-Bragg). The TM gaps aren't used for the nomenclature as they always sit within the TE gaps and their topology only differs in that they close at the Brewster condition $\tilde{n} = n_B = n_i \sin(\theta_B)$ (§ A.2.1.2).

a TE gap closure point in the *high-frequency* direction will *increase* the gap l index by 1 and *reduce* the m index by 1. All gaps shown in Figs. 2.8 and 2.9 are labeled using this system.

The ability to generate this bandgap taxonomy is critical in that it allows one to uniquely identify a particular gap for any layer configuration. Beyond this, § 3.7.1 demonstrates how the nomenclature is actually inextricably and invaluably linked with the underlying physical behaviour of such bandgaps.

As will be demonstrated in § 3, all gaps terminating on the $\tilde{n} = 0$ and/or $\tilde{n} = n_0$ lines are topologically open, whereas all other gaps are closed. It is the open nature of the gaps terminating on the n_0-light-line (the $\langle l, 0\rangle$ gaps) that is responsible for their remarkably large bandwidth and hence for the novel guidance properties of air-Bragg fibres; there are clear parallels here to the bandgaps and guidance of conventional 2-D bandgap fibres [2, 3] which are widest on the low-index light-line. Incidentally, one can now identify the fundamental and second-order gaps as $\langle 1, 0\rangle$ and $\langle 2, 0\rangle$, respectively. Gaps with $m > 0$ can strictly only be accessed by Bragg fibre configurations with $\tilde{n} < \{n_1, n_0\}$; typically the case for $n_{\text{core}} < \{n_1, n_0\}$ (the basis of Chapter 3).

2.6 Reducing Confinement Loss

The observation that $CL_{\min}$ is lower in higher order $\langle l, 0\rangle$ gaps than in the fundamental $\langle 1, 0\rangle$ is a general one. This applies to any fibre with a sufficiently large core radius a such that $\text{Re}\{\tilde{n}(\lambda)\}$ intercepts the $\langle 2, 0\rangle$ gap. To see this, take the $n_0 = 1$ example where the tube analogy is again made: one can see how any given mode's $\text{Re}\{\tilde{n}\}$ is increased towards its asymptote at n_0 for increasing core radius a since, as per Eq. 2.1, $1 - \text{Re}\{\tilde{n}\} \propto \lambda^2/a^2$. § 2.4 presents one such case of this use of these wide bandgaps. Other air-Bragg fibre configurations may vary in core radius a, global scale factor G, cladding layer thickness ratio $\frac{t_1}{t_0}$, substrate refractive index n_1, or the total number of cladding rings pairs N. For all cases, higher order bandgaps will always exist and produce a lower $CL_{\min}$ for the reasons discussed above[9].

Reduction of confinement loss of an idealised air-Bragg fibre at a given wavelength, without introducing extra structural complexity such as increasing the number of cladding rings, is now investigated. Here this is done for $\lambda \approx 1155$ nm: the wavelength of the considered air-Bragg fibre's $CL_{\min}$. There are two ways to do this: by exploiting a

[9] Konorovet al. [156] indirectly demonstrate an example of this generality with the calculation of the CL spectrum of an air-Bragg approximation to a 2-D hexagonal HC-MOF in which many higher-order gaps are calculated and shown to have decreasing $CL_{\min}$ towards shorter λ.

higher-order bandgap; or by increasing the size of the core. As discussed above, both techniques essentially bringing $\tilde{n}$ closer to the light-line, which generally reduces CL.

The first technique requires spatially scaling the whole geometry up to shift the position of the $\langle 2,0\rangle$ gap's relatively lower $CL_{\min}$ ($\lambda = 480$ nm) to that of the fundamental ($\lambda \approx 1155$ nm). This method is possible from the scale invariance of the problem: since none of the fibre parameters depend on λ (ignoring material dispersion here), by scaling λ and the geometry by the same factor, $\tilde{n}$ must be invariant, thus CL is also invariant to within an inverse factor of the spatial scaling factor[10], seen directly from a unit analysis: $[CL] = m^{-1}$. This type of global scaling can be almost trivially implemented during the fibre drawing process, say, by altering the drawing speed, temperature or internal pressure. This is the principal reason this scaling approach to CL reduction would be so appealing. Indeed, it also allows one to fabricate a fibre whose fine structural details are larger, hence typically easier to fabricate, than those of one which guides within the fundamental bandgap requiring smaller dimensions.

Scaling only the core radius a of the fibre, keeping all other structural parameters constant, can be implemented to reduce the $CL_{\min}$ of the fundamental gap itself, without significantly shifting its position. This method works because, by increasing a, $\mathrm{Re}\{\tilde{n}\}$ approaches n_0. As discussed, this is explained via the tube analogue: Eq. A.177 describes how $\beta \to k_0$ ($\mathrm{Re}\{\tilde{n}\} \to n_0$) monotonically as $a \to \infty$. Fig. 2.9 explicitly shows this, with the $\mathrm{Re}\{\tilde{n}\}$ of the $\mathrm{T(E/M)}_{01}$ modes of a tube analogue for a range of a overlayed on the bandgap maps. It is interesting to note that CL reduction via increasing core size has also been considered for conventional, hexagonal/trigonal lattice cladding, PBGFs [16].

The results in Fig. 2.10, calculated for the TE_{01} mode via the cTMM, demonstrate the scaling of $\mathrm{CL}(\lambda)$ within the $\langle 1,0\rangle$ gap with respect to the core radius a (top) and the shifting of the $\langle 2,0\rangle$ gap's $\mathrm{CL}(\lambda)$ curve position with respect to the global scale factor G (bottom). The scale factor multiplies the structural dimensions of the fibre by the same amount in each dimension, *e.g.*, $G = 1$ produces the original structure and $G = 2$ doubles the size of the whole structure.

Fig. 2.10 (top) demonstrates the expected $1/G$ relation between $CL_{\min}$ in the second-order gap and the global scale factor: $CL_{\min}$ decreases to 1.63×10^{-7} dB/km as its position is shifted, along with the entire $\langle 2,0\rangle$ gap, to $\lambda = 1.155$ μm—noting that it was already much lower than the $\langle 1,0\rangle$ gap loss to begin with. The scale factor required for this is $G = 2.4$. Note that this is greater than a factor of 2: the scale factor that would be implied by considering only an antiresonance model, implied from the forms of

[10] By the same reasoning, all calculations considered here thus also describe the behaviour of all similar waveguides related via a global scale factor to the one considered (a simple but important point).

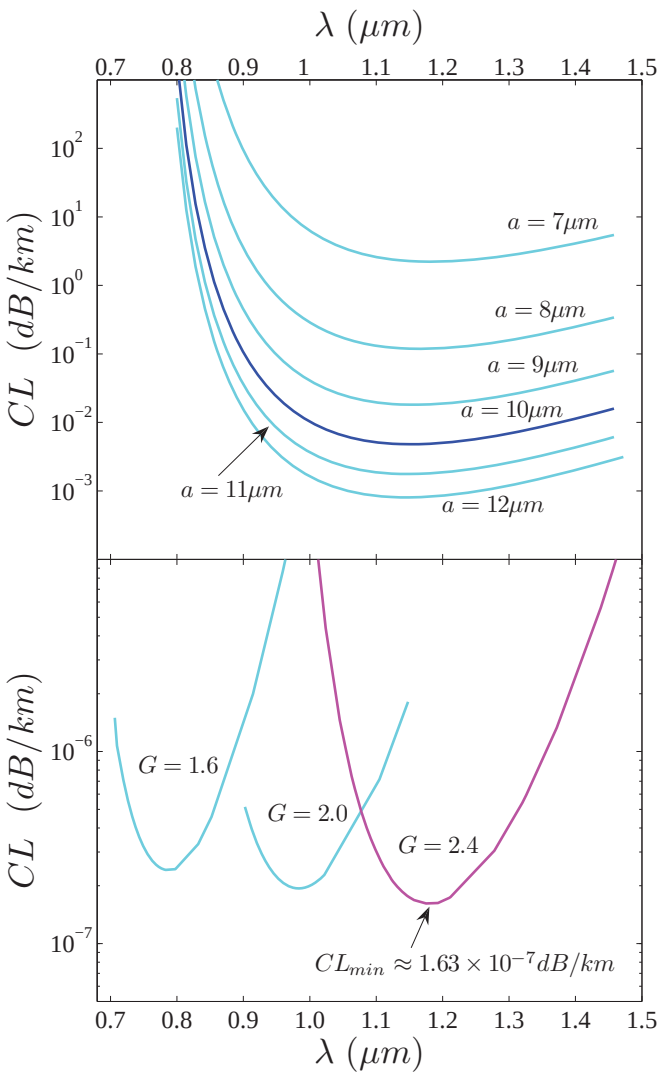

FIGURE 2.10: The TE_{01} mode calculated by the TMM. *Top*: CL of the TE_{01} mode in the $\langle 1,0\rangle$ gap a range of core radii $a = 7\ \mu\text{m} \rightarrow 12\ \mu\text{m}$. The original radius $a = 10\ \mu\text{m}$ corresponds to the solid curve. *Bottom*: CL for the $\langle 2,0\rangle$ bandgap for global scale factors $G = 1.6$, 2.0, and 2.4. The solid curve corresponds to G shifting the $\langle 2,0\rangle$ gap's CL_{min} to $\lambda = 1.155\ \mu\text{m}$ (the $\langle 1,0\rangle$ gap's CL_{min} position when $G = 1$).

λ_m and $\lambda_m^{\text{antires.}}$ above. The full CL and antiresonance models depart here for the same reasons the antiresonance points and CL_{min} position don't align as described earlier: the band edges provide a more accurate description of the low-loss regions rather than the layer resonance approximations.

In order to produce a similarly low CL_{min} using the $\langle 1,0\rangle$ gap, a must be increased significantly. Fig. 2.10 (bottom) shows that CL_{min} within the fundamental gap initially exhibits an extremely rapid decrease in its rate of change for increasing R. This is explained by observing the position of the equivalent tube dispersion curves with respect to the bandgaps as shown in Fig. 2.9: as *a decreases* from 10 μm, $\text{Re}\{\tilde{n}(\lambda)\}$ shifts down and enters a *smaller* region of the $\langle 1,0\rangle$ gap. As the available bandgap region decreases,

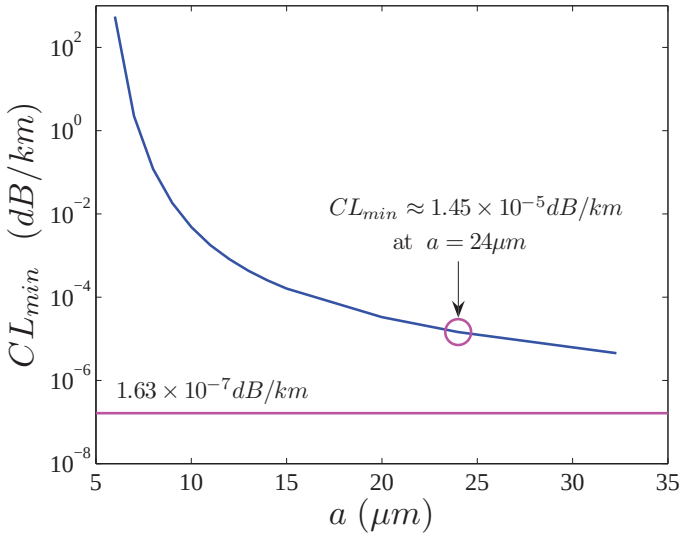

FIGURE 2.11: *Blue curve*: CL_{min} of the TE_{01} mode in the $\langle 1,0\rangle$ bandgap for a range of core radii. *Magenta line*: CL_{min} of the TE_{01} mode obtained by scaling the entire fibre structure (by G) such that CL_{min} in the $\langle 2,0\rangle$ gap is shifted to the position of CL_{min} in the original (unshifted) $\langle 1,0\rangle$ gap; this corresponds to a global scale factor of $G = 2.4$.

CL_{min} is affected by both the encroaching band edges *and* the fact that the mode is moving away from the n_0-light-line. Both these effects see that CL_{min} *increases* rapidly as a is *decreased*, as demonstrated in Figs. 2.10 (top) and 2.11. As a *increases*, however, $\text{Re}\{\tilde{n}(\lambda)\}$ approaches the light-line at a slower rate; relating to the tube analogue again, this is due to the reciprocal relationship $1 - \text{Re}\{\tilde{n}\} \propto 1/a^2$ from Eq. A.177. Since this decreased rate of approach also occurs within a region where the band edges don't change significantly, CL_{min} decreases slowly, as demonstrated by the tail of the curve in Fig. 2.11.

Global scaling of the whole structure to exploit the second-order bandgap is thus an effective means of reducing CL at a desired wavelength, embodied in Fig. 2.11: a scale factor of $G = 2.4$ shifts the $\langle 2,0\rangle$ gap to $\lambda = 1.155$ μm giving $CL_{\text{min}} = 1.63 \times 10^{-7}$ dB/km, whereas increasing a by the same scale can only produce $CL_{\text{min}} = 1.45 \times 10^{-5}$ dB/km within the $\langle 1,0\rangle$ gap. In order to achieve the same CL_{min} via increasing r_{core} as by shifting the $\langle 2,0\rangle$ bandgap, an impractical core radius of $a \approx 1mm$ would be required (beyond the axes of Fig. 2.11 by 3 orders of magnitude). Exploiting the higher order bandgap in this way provides a real advantage in terms of fabrication since scaling of the fibre structure during the drawing process is much easier to implement than significant scaling the core radius alone. As mentioned earlier, a global scaling of the structure requires only the variation of fibre drawing parameters such as temperature and draw speed, say. Increasing the core radius dramatically, however, is much more difficult, especially when maintaining the same cladding dimensions; the resulting large core size to

cladding pitch ratio $a : \Lambda$ would require much extra care during the fabrication process (extreme differences in hole sizes being very hard to fabricate due to the large pressure gradients between holes of disparate sizes). Also, many more supporting struts would be required to hold together the rings—the volume of air between adjacent rings becoming larger as their radius increases.

Also, by avoiding a significant increase in core size, the exploitation of higher-order gaps makes asymptotic single-modedness much easier to achieve; smaller core radii produce fewer core-modes within the desired bandgap and hence fewer modes with loss low enough for practical guidance.

For completeness, it is noted that in using this method, the $\langle 2, 0 \rangle$ gap can be shifted to the popular wavelength $\lambda = 1550$ nm using a scale factor of $G = 3.23$, producing $CL_{\min} \approx 1.21 \times 10^{-7}$ dB/km for the TE_{01} mode.

2.7 Struts and Polygonal Geometries—Modal Analysis

Here the confinement loss properties of the lowest order core modes, TE_{01}, TM_{01} and HE_{11}, are analysed for variations to an idealised structure to which connective struts have been added in various configurations and in which the rings have been transformed from annular to hexagonal. This is done for a few reasons: to analyse the effect of connective struts and their number and distribution on modal confinement loss; to analyse the influence of the shape of the cladding rings on the modal behaviour; and the use of the latter to justify the investigation of polygonal air-Bragg fibres, fabricable via an extrusion technique, say—critical to the motivation of Chapter 5.

The finite element method is used for this analysis since it is sufficiently flexible to make the eigen-analysis of such complex geometries soluble, as discussed in § 2.3.4. The waveguide structures upon which it was used are represented with their calculated confinement loss spectra in Fig. 2.12 (overleaf).

2.7.1 Fibre Structures and Model Parameters

The air-Bragg structures considered here are based on the structure considered by Foroni et al. [71, 72] in which a FEM was also used to calculate the modal properties of an air-Bragg fibre. The structure considered was based on the fabricated 'OD90' air-Bragg fibre structure of Vienne et al. [43] and will be referred to as the *Vienne-structure*.

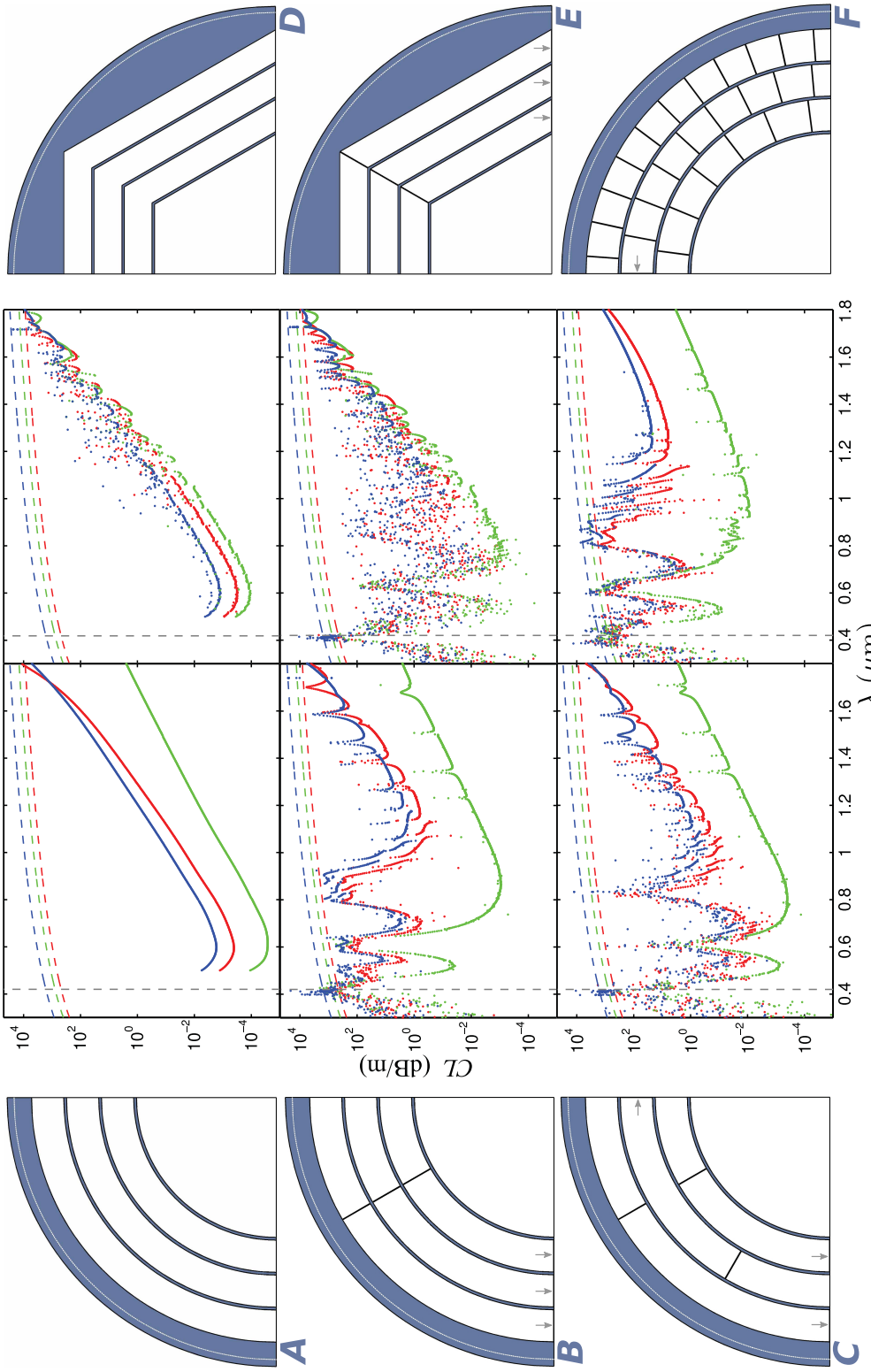

FIGURE 2.12: Confinement loss spectra for a range of annular and polygonal air-Bragg geometries with and without struts. All geometries (labelled $A \rightarrow F$) have the same ring air-layer and strut thicknesses, core diameters and refractive indices, discussed in the text. *Red points:* HE_{11} mode. *Green points:* TE_{01} mode. *Blue points:* TM_{01} mode. *Dashed coloured curves:* CL curves of the equivalent tube waveguide (colours are the same as the FEM calculated modes). *Vertical dashed grey line:* position of the first-order resonance of a high-index cladding ring. *Grey arrows:* positions of a (half) strut which is obscured by the boundary of the reduced domain. *White dotted line:* boundary of the PML region of the modelled structure.

The Vienne-structure consists of concentric annular rings connected by the (realistically required) bridging struts. The geometrical parameters were: core diameter $D_{\text{core}} = 20\ \mu\text{m}$, strut thickness $t_{\text{strut}} = 45$ nm, glass ring thickness $t_{\text{ring}} = 200$ nm, air gap thickness $t_{\text{air}} = 2.3\ \mu\text{m}$, number of binary cladding layer pairs $N_{\text{pairs}} = 3$. These same parameters are use here.

In order to produce a geometry that exhibits 4-fold symmetry, making it possible to truncate the geometry to a quarter plane to reduce the calculation complexity (as discussed in § 2.3.4), the number of struts in each air region is approximated by an even integer (differing from the real OD90 fibre by a few struts per ring). From the inner ring to the outer ring, for a full (non-truncated) structure, the number of equally azimuthally spaced struts in the first to final air rings is 24, 34 and 44, respectively (as used in Refs. [71, 72]). The struts are orientated with respect to each so as to produce the maximum symmetry possible: $C_{2\nu}$ group symmetry (2 mirror symmetries and one rotational [184]) in which the quarter-plane truncation contains 6, 8.5 and 11 struts in the inner to outer air gaps, respectively (shown in Fig. 2.5 and Fig. 2.12-*F*).

As described in § 2.3.4, the appropriate boundary conditions for the internal terminated boundaries (the symmetry planes of the truncated structure) must be employed in order to solve for the mode classes containing the TE_{01}, TM_{01}, or HE_{11} modes (requiring perfect electric, perfect magnetic, and combinations of the two, respectively). The HE_{11} mode here was calculated using a perfect electric boundary condition on the vertical internal boundary (Fig. 2.5 and Fig. 2.12-*F*) and perfect magnetic conditions on the horizontal (swapping the two produces a very similar mode with only very subtle modal differences that exist due to the way the struts are distributed—they produce 2, not 4, mirror symmetries).

Here, sharp edges are made between the rings and the struts; no rounded corners are used to approximate a fabricated structure. This is done predominantly for simplicity of systematic analysis since such rounding is a deviation from the simplest representation. As shown in Ref. [72], by incorporating rounded edges into the Vienne-structure model, the calculated CL spectrum is shifted by 200 nm to longer wavelengths—possibly due to the increased high-index material in the cladding increasing the average refractive index in the low-index (air-hole) cladding layers, shifting the effective bandgap or resonances. Nonetheless, the qualitative details of the model are left intact by ignoring the rounding and is satisfactory for the analysis here since the qualitative behaviour is of most interest.

Maximum mesh element sizes generated over the structure are as follows: glass regions, 0.1 μm; core region, 0.2 μm; and PML region, 0.1 μm. The PML annulus has a thickness of 1 μm. The air regions in the cladding have maximum element sizes of $\approx 0.2\ \mu\text{m}$ but are automatically generated by COMSOL's advanced mesh generation routines (*i.e.*,

a maximum element size isn't strictly enforced). Using these mesh parameters, the models required a total of $\sim 10^4$ mesh elements. As discussed earlier, a single iteration with this number of mesh elements takes about 10 minutes to complete. Since each of the calculated spectra shown in Fig. 2.12 contains about 1000 points, the spectral calculations for each mode required a calculation time of at least a week (requiring a total computational time of about a month—all modes must be calculated separately due to the unique boundary conditions of each mode type). The computer system used for these calculations is the same as described earlier in § 2.3.4 in the discussion of the finite element method implementation.

The other structures considered are variations on the Vienne-structure, all shown in Fig. 2.12, labelled $A \rightarrow F$. Fig. 2.12-A is for an idealised version of the Vienne-structure in which all struts have been removed, leaving the concentric annular rings. Fig. 2.12-B incorporates 6 *colinear* struts in each air ring (1.5 within the quarter-plane). Fig. 2.12-C is identical to Fig. 2.12-B but employs *offset* struts such that the struts in each ring are azimuthally offset from those in the adjacent ring by $\pi/6$. Fig. 2.12-D is the same as the idealised Vienne-structure (Fig. 2.12-A) but where the annular rings have been replaced with hexagonal rings (the edges of the hexagonal rings are as far from the centre of the fibre as the idealised version's annular rings' radii, *i.e.*, if overlayed the edges of the circular rings would fit within the edges of the hexagonal rings, not vice versa). Fig. 2.12-E is identical but incorporates 6 colinear struts (1.5 in the quarter-plane geometry) that coincide with the apexes of the hexagonal rings. Fig. 2.12-F is the Vienne-structure itself, as described above.

2.7.2 Numerical Results

Here, the confinement loss spectra calculations for the TE_{01}, TM_{01} and HE_{11} modes for all considered structures will be discussed with inferences of the CL features made with respect to its parent fibre structure. $\mathrm{Re}(\tilde{n})$ is not considered here since the curves of all modes tend to deviate only slightly from their tube analogues (in the same way the Bragg fibre and tube mode dispersion curves were related in the previous sections). For these investigations into the influence of the cladding structure upon mode guidance, CL is the most appropriate and revealing as it is directly related to the radially propagating power that manages to make its way through the cladding structure, as per Eq. A.27, making subtle interactions with the cladding obvious.

This section will be split into two main topics: the discussion of novel confinement loss phenomena calculated for the Vienne-structure once all modes are considered; and the influence of the distribution of cladding struts and the shape of the cladding rings.

Novel Confinement Loss Phenomena

The first observation to make is that the HE_{11} mode CL spectrum for the Vienne-structure (Fig. 2.12-*E*) is, as far as can be told from investigating the plots, very close to that calculated by Foroni et al. [71, 72]. This is useful for a 'sanity-check' in that it appears the FEM model can replicate the modal properties of the (particularly complex) full Vienne-structure. From this, the validity of the calculations of the other modes and structures is implied (since the HE modes effectively contain both TE and TM components—hence the mixed terminal boundary conditions—and the other structures are geometrically more simple).

One thing to note about the results of Refs. [71, 72] (and indeed all[11] references on the numerical modelling of this air-Bragg fibre [70, 73]) is that only the HE_{11} mode is calculated[12]. As noted in Ref. [72], the Vienne-structure produces a CL spectrum much higher than the idealised (no strut) equivalent structure. This is seen explicitly in comparing the calculations here between Fig. 2.12-*F* and Fig. 2.12-*A*. Not only is the loss significantly increased (by about 4 orders of magnitude) by introducing the struts of the Vienne-structure, but the CL minimum is shifted to longer wavelengths: the CL curve appears relatively smooth (save for some thin loss peaks—surface mode couplings according to Ref. [72]) down until the CL rapidly increases as if it has encountered a strong resonance at about $\lambda \approx 0.85$ μm. There appears to be another similar strong loss feature at about $\lambda \approx 0.62$ μm; between these two features the loss drops (to an even lower value) as if the two features were indeed strong cladding resonances. There is also a smaller resonance-like feature (not as visually obvious as the first two) at $\lambda \approx 0.5$ μm. None of these high-loss regions coincides with a resonance of the annular cladding rings since the only ring resonance in the calculated domain is plotted on top of this data and sits at precisely $\lambda = 0.42$ μm (calculated as per the antiresonance analysis of § 2.3.3). These resonance-like features were not clearly defined in the results of Refs. [70–73] (often being excluded from the displayed results) possibly due to insufficient numerical accuracy[13], although one can make out the features within the noise such as in the inset to Fig. 4 of Ref. [72], say.

[11] Save for Ref. [69] which considers all three but only for a single wavelength.

[12] Except for the results in Fig. 6 of Ref. [72] where the TE_{01}, TM_{01} and HE_{11} modes are shown for Vienne-structure with rounded edges. However, there the CL spectrum is restricted to the domain of the shown HE_{11} mode (which excludes the novel resonance-like features discussed here) and so it is unclear as to whether the observations made here could be made of their model, too; keeping in mind the rounded edges can effect the CL spectrum, as discussed within.

[13] This is justified by the fact that the CL spectrum for the idealised geometry shown in Fig. 4 of Ref. [72] has a moderately 'noisy' structure. The idealised geometry should only produce a smooth CL curve as shown here in Fig. 2.12-*A*, or in Figs. 2.6 and 2.8 where the FEM is compared to excellent precision with a semi-analytic cTMM. Any 'noisy' deviations indicate that the model employed contains inaccuracies (due to a coarse FEM mesh or boundary absorber parameters producing insufficient convergence, say.).

Clearly something interesting is occurring upon introduction of the struts which is in addition to the resonance effects of the cladding rings. It is unclear as to whether these resonance-like features are due to the surface mode anti-crossings (symmetry-induced couplings) that are responsible for the fine peaks seen throughout the CL spectra, as characterised by Ref. [72]. Since the surface mode interruptions appear to become more severe as shorter wavelengths are approached (Fig. 2.12-*F*), this is a possibility that warrants further investigation. However, surface modes need not be the only explanation. During the calculations of these CL spectra it was observed that some of the fine loss peaks were not associated with a surface-mode anti-crossing: some of the small CL peaks exist in the absence of an interaction with surface modes (evidenced by the lack of core-to-surface evolution observed during simulations about these points). Some of these loss features could thus be due to nontrivial resonances with the cladding structure, rather than symmetry-induced anti-crossing interactions with cladding modes. This, too, warrants further investigation.

In order to analyse the guidance properties further, the TE_{01} and TM_{01} modes were also calculated for all structures (instead of just the HE_{11} mode as in Refs. [70–73]). Staying with the Vienne-structure for now, Fig. 2.12-*F* demonstrates how the TM_{01} mode has very similar CL behaviour to the HE_{11} but the TE_{01} mode is markedly different.The fact that the HE_{11} mode closely follows the loss characteristics of the TE_{01} has been seen and explained earlier (§ 2.4) in the context of an idealised air-Bragg fibre: the effective TM components of the HE_{11} mode sees it dominated by the loss characteristics enforced by the TM components. This is seen directly here, too, in that, just as for the idealised structure in Fig. 2.12-*A*, the HE_{11} mode's CL spectrum has a values closer to the TM_{01} mode than the TE_{01} mode.

Given these observations, note how extremely different the TE_{01} mode's CL spectrum is to the other modes for the Vienne-structure (Fig. 2.12-*F*): the resonance-like features at $\lambda \approx 0.62$ μm and 0.5 μm are *absent*. In particular, the absence of the 0.8 μm feature allows the TE_{01} mode's CL to drop down closer the value of its idealised analogue (Fig. 2.12-*A*) than was possible for the other modes. A similar, but less striking, observation is made for the feature at 0.5 μm. Clearly, then, these resonance-like loss features are *polarisation dependent*; the azimuthally-pointing (up to vector effects at the structure interfaces) nature of the TE_{01} mode negates its interaction with whatever is responsible for this loss feature. It would seem that this is a vital observation for the investigation of these novel confinement loss features.

As was mentioned in § 1.2.3, the HE_{11} mode CL calculations of Refs. [70–73], and hence also the calculations here, do not appear to match with the observed bandwidth and position of the experimentally measured transmission spectra of Ref. [43]. Not only

that, but the minimum calculated CL of the HE_{11} mode ($\sim$ 10 dB/m) is rather higher than the nominal measured loss of ($\sim$ 1 dB/m), implying that the broader bandwidth of the calculated mode would be well above this measured value by about two orders of magnitude or more.

One could then argue that modes of predominantly TE field content have a broader bandwidth at low CL and could thus be responsible for the broader experimentally measured transmission spectrum and the position of its transmission maximum. Indeed, since the resonance-like feature at $\lambda \approx 0.85$ μm is absent from the TE_{01} spectrum, it is able to reach a minimum CL $\approx 8.5 \times 10^{-3}$ dB/m (at $\lambda \approx 0.92$ μm), well below that of the nominal measured value, leaving a reasonable amount of headroom for the broader bandwidth of the CL spectrum to accommodate for the wider measured transmission spectrum.

In fact, if one inspects Fig. 4 (a) of Ref. [43], it will be noted that the measured spectrum of the OD90 fibre (which these models are an approximation to upon) appears to follow the trends of the TE_{01} mode CL spectrum calculated here (Fig. 2.12-*F*): the transmission spectrum reaches its peak at $\lambda \approx$ 1 μm, which is where the calculated TE_{01} CL minimum occurs; this peak drops off rapidly but then rises again on the short- and long-λ sides, possibly due to the predominance of the TM_{01} and HE_{11} CL minima which occur at about these positions; what was attributed to a "second-order peak" (as in: a second-order bandgap or cladding ring resonance) in Ref. [43] at $\lambda \approx$ 500 nm could indeed be due to the combined CL minima bound between the fundamental cladding ring resonance and the short-λ resonance-like feature at $\lambda \approx 0.62$ μm in Fig. 2.12-*F*. While modelling of a more faithful structure to the fabricated one is required (rounded corners at the strut-ring junctions, say) these results go a long way to potentially explaining the nontrivial transmission spectrum of these fibres, and certainly further than just considering the HE_{11} mode alone. Further investigations should consider the properties of higher-order core modes and their resonant effects with the cladding structure as well as the influence of cladding modes.

In summary, one can conclude that:

- the Vienne-structure exhibits at least three novel resonance-like high-loss features in the confinement loss spectra of the TM_{01} and HE_{11} modes (and hence likely all modes with TM content),
- the TE_{01} is not affected by two of these features, allowing it to span a greater bandwidth at much lower loss than the TM_{01} or HE_{11} modes,
- these two comments imply that the resonance-like features are polarisation dependent (insofar as the TE and TM content of the full-vector fields of the leaky modes is concerned),

- the experimentally observed transmission spectra of which the model of Fig. 2.12-*F* approximates can potentially be explained by the markedly different behaviour of the calculated mode types, particularly the low, broad-band, loss spectrum of the TE_{01} mode,
- and by investigating the origins of these loss features, one might be able to suppress them for certain mode types (such as those with TM content) by altering the air-Bragg design in some way.

The Effects of Strut Distribution and Ring Shape

The behaviour of the variants to the Vienne-structure shown in Fig. 2.12 are now discussed. These variants are based upon different distributions of the cladding struts and the alteration of the cladding ring shape from concentric annuli to hexagonal rings. They will now be discussed in order from Fig. 2.12-*B* to Fig. 2.12-*E*.

Structure *B* is a variation to the Vienne-structure that has only 6 struts per air ring (1.5 in the quarter-plane) which are radially aligned (colinear). The first observation to make regarding the computed confinement loss structure of this fibre geometry is that it is remarkably similar to the full Vienne-structure. All of the aforementioned novel resonance-like features exist for the TM_{01} or HE_{11} modes at the same positions and with the same spectral widths as for the Vienne-structure. Also similar is the fact that the TE_{01} mode does not succumb to the high-loss features at $\lambda \approx 0.85$ μm and $\lambda \approx 0.5$ μm. One can thus make the same arguments as above with respect to the these features being polarisation dependent and their absence for the TE_{01} mode allowing it to reach a lower minimum CL than the other modes. In fact, the TE_{01} mode for structure *B* reaches a minimum CL of $\approx 9 \times 10^{-4}$ dB/m (at $\lambda \approx 0.87$ μm) which is an order of magnitude lower than for the full Vienne-structure. This lower confinement loss could be due to the fact that the reduction of struts in the cladding naturally reduces the average refractive index of the low-index (air-hole) layers such that the core modes move closer to the effective low-index light-line of the cladding, reducing the confinement loss (in the same way it was discussed how core modes approaching the light-line have low loss in the previous sections). In the sense that the cladding struts could manifest as an average layer index and contribute to the effective bandgap behaviour in this way, the Vienne-structure is potentially similar to an average-index Bragg fibre [66] as discussed in § 1.2.2. The removal of struts has the effect of moving the fibre structure conceptually closer to a level-core Bragg fibre in that the average refractive index of the cladding region is reduced to essentially that of air (the same as the core), reducing the minimum CL.

Important for the justification of the spider-web geometry, introduced in § 1.4 and demonstrated experimentally (and compared with theory) in Chapter 5, is the fact that the colinear nature of the supportive struts does not seem to have the effect of increasing the confinement loss any more than their mere presence does. One could argue that in having the struts aligned, they allow light to be tunnelled through them and out into the jacket region much more easily than if they weren't colinear. Indeed, when the struts are offset as much as possible (so that the end of each strut is as far from the one in the adjacent layer as possible), as for the structure *C* in Fig. 2.12-*C*, one can see that, if anything, the offset struts disrupt the CL spectrum more than the colinear ones do (discussed further presently). This apparent lack of a significant tunnelling effect may very well be due to the fact that the struts are quite thin (45 nm thickness), well below the wavelengths considered here; the effect of tunnelling could be investigated further by scaling the strut thickness in these models. Ref. [71] considers the effect of altering the thickness of the struts of the full Vienne-structure from 45 nm to 70 nm, demonstrating an increase in CL (as would be expected for increased tunnelling) but coupled with a significant shift in the position of the minimum CL. This latter effect indicates that the effect of increasing the thickness of the struts in the Vienne-structure increases the average-index of the low-index rings, hence altering the effective bandgap/resonance positions. In order to determine the effect of tunnelling further, the average-index effect (if that is the mechanism responsible) should be suppressed by considering structures with fewer struts, like those considered here. This suggests future work to consider for these few-strut models.

Structure *B* has a significantly 'cleaner' CL spectrum than the Vienne-structure, especially for the TE_{01} mode; the CL curves of all modes exhibit fewer interruptions along the calculated range of wavelengths. This implies that, perhaps unsurprisingly, the reduced number of struts produces fewer surface-mode couplings (as per Ref. [71, 72]) and nontrivial cladding resonance (as discussed above). Reduction of the number of struts even further (to 4 or 2 per layer, say) thus appears to be a means of isolating the novel resonance-like features from the more fine-grained surface mode type interactions that disrupt the CL spectra in an effort to better understand the various loss mechanisms at play.

Structure *C* (Fig. 2.12-*C*, just discussed) is an identical structure to structure *B* (6 struts per air ring—1.5 in the quarter-plane) but where the colinear struts have been modified to be offset from each other. More precisely, the struts of the second ring are azimuthally offset from those in the adjacent rings by a $\pi/6$ rotation. The first obvious effect of offsetting the struts is the increase in the number of interruptions to the CL spectra the TM_{01} and HE_{11} modes, likely due to an increase in surface-mode anti-crossings. However, the TE_{01} mode CL spectrum appears almost unchanged when

compared to its colinear strut counterpart. Thus, whatever the reason for the increase in loss features of the other modes, the TE_{01} mode appears to be unaffected. Perhaps, then, given the predominance of this effect and the large resonance-like features (at $\lambda \approx 0.85$ μm and 0.5 μm) for only the TM_{01} and HE_{11} modes, one could suggest that the effect of offsetting the struts is also polarisation dependent in the same sense (and possibly under the same mechanism) as the resonance-like features.

Another noteworthy feature of loss of structure C compared to B is that the width of the large resonance-like features at $\lambda \approx 0.85$ μm, 0.62 μm and 0.5 μm all appear to the 'sharper' in that their width seems to be reduced to a point. This appears to have the effect of lowering the minimum loss between them for all modes as well. Thus, while offsetting the struts appears to introduce many more fine loss features to the CL spectra of the TM_{01} and HE_{11} modes, the widths of the large resonance-like loss features are reduced for all modes. This suggests that the broadness of the large loss features depends upon the proximity of adjacent struts since these features appear to be occupy the same range of wavelengths for structures B and F (which have struts in adjacent rings close to one another) but occupy only a very small (possibly singular) wavelength when the struts are maximally offset.

Structure D represents a deviation from annular rings to hexagonal rings. It is the same idealised (strutless) structure as A but with hexagons replacing the circular ring edges such that the shortest distance from the centre of the core to the hexagons is equal to the radius of the original annuli (*i.e.*, the circles fit within the hexagons). This structure is thus very similar to that considered by Pearce et al. [145], discussed in § 1.2.2, in which they used a FEM to model the modal confinement loss properties of a structure consisting of concentric hexagons; the principal difference with their structure, however, was the inclusion of a hexagonal core ring which was rotated by $\pi/3$ in order to best approximate a Kagomè fibre (neglecting the interstitial struts). It is unsurprising, then, that one should also observe that the CL spectrum of structure D exhibits surface-mode style interruptions that increase in number and severity toward the edges of the CL curve, as was shown for the structure of Ref. [145]. These loss features appear in the absence of connective struts, so their existence cannot be attributed to the arguments above (based on the surface-mode results of Ref. [71, 72]), and were explained in Ref. [145] as being due to surface modes induced by the corners of the polygonal rings. This is possible since, like the inclusion of the connective struts, the corners of the polygonal rings breaks the cylindrical symmetry of the waveguide, providing a defect with which to induce symmetry-based mode coupling (anti-crossings) with surface modes.

Polygonal rings, like colinear struts, are also important for the motivation of the spider-web fibre design. This is because, by having only a few colinear struts in the design,

annular rings would not hold their shape under the surface tension effects of fabrication, as will be demonstrated and discussed in Chapter 5. This 'straightening out' of the ring edges is unavoidable for any air-Bragg structure hoping to employ reasonably spaced struts.

Note also that the TE_{01} mode of structure *D* has CL generally raised closer to that of the TM_{01} and HE_{11} modes compared to the equivalent annular case (structure *A*), even though the TM_{01} and HE_{11} modes appear unchanged between the two structures save for the surface mode effects. This is likely because the low-loss behaviour of the TE_{01} mode is due to it field configuration at the cladding ring boundaries [171]. The TE_{01} mode's electric field is everywhere tangential to the cladding ring boundaries in a Bragg fibre with circular rings. When these rings are disrupted from such a prefect circle, the TE_{01} mode cannot maintain this constant boundary condition over the entire ring; the loss follows suit. Nonetheless, it is clear that the TE_{01} is still the lowest loss mode for the polygonal structure and, importantly, that the loss is not increased beyond an order of magnitude buy replacing annular rings with hexagonal ones.

Structure *E* is identical to *D* except that connective strut have been included. The struts are the same width (45 nm) as those in the previous structures and lie along the vertices of the hexagonal rings. Naturally, in this case the struts must be colinear in order to approximate a fabricable structure (as discussed above). This structure is thus most reminiscent to a spider-web fibre, consisting of concentric polygonal rings supported by connective struts.

The effect of adding the struts to the hexagonal structure is considerable: all modes' (particularly TM_{01} and HE_{11}) CL spectra become 'noisy' in that the CL values rapidly fluctuate as that follow a general trajectory similar to that of the strutless case. This noisy CL behaviour is very similar to that calculated for a Kagomé structure in Ref. [145]. The similarities between the Kagomé structure this spider-web type structure are thus quite deep. It is unclear as to why the addition of struts to the hexagonal rings produces this noise effect when it is not observed for the addition of struts to the annular case, highlighting another avenue for investigation.

One can also note that all of the major novel resonance-like CL features are present in the modes of structure *E* just as for all of the other strut-laden structures considered here. This includes the polarisation dependence of the loss features since the TE_{01} mode once again appears to be unaffected by the loss features at $\lambda \approx 0.85$ μm and 0.5 μm. In this sense, the fibre structure still produces behaviour very much like the Vienne-structure and its variants.

For experiment, the noisy CL spectrum is likely of little concern. Indeed, Kagomè fibres have already been demonstrated as an emerging platform for hollow-core guidance and their transmission spectra and dispersion profiles appear not to exhibit such rapid fluctuations (*e.g.*, see the references in Table 1.2). As argued later in § 5.5, this discrepancy between rapid CL fluctuations and experimental observation could be explained by the fact that fabrication tolerances during the fibre fabrication process would see the small structural fluctuations along the length of a fibre smooth these fine features out as they are shifted over one another as the light propagates down the fibre length. In other words, it would be very hard to maintain such fine spectral features in a fabricated waveguide.

In summary, one can conclude that:

- the addition of struts in general (circular or hexagonal alike) induces large, anomalous, polarisation dependent resonance-like features in the CL spectra,
- reducing the number of struts in the cladding reduces the minimum CL of all modes (possibly due to many struts raising increasing the average refractive index of the air-hole layers),
- offset struts produce more well-defined anomalous resonance-like CL features (which reduces the minimum CL of all modes),
- colinear struts produce 'cleaner' CL spectra than offset struts,
- the TE_{01} mode is barely affected by the transition from colinear to offset struts, again indicating its indifference to possible polarisation dependent resonance effects of the cladding,
- hexagonal structures (and thus likely polygonal structures in general) exhibit many of the same general modal features, and exhibit very similar minimum loss values for all modes, as their circular counterparts both with and without connective struts,
- the addition of struts to the hexagonal structure ($D \rightarrow E$) converts the comparably smooth, Bragg fibre like, CL spectrum into a 'noisy' spectrum as calculated for Kagomé fibres (but still maintaining the predominant CL features of the circular equivalent structures).

Of course, all geometries presented here that include struts must be exhibiting a Von Neumann Wigner type guidance mechanism, permitting the confinement of light to the low-index waveguide core in the absence of a true cladding bandgap: low-loss core modes can co-exist with the cladding modes (see § 1.2.3 and Fig. 1.6). It is clear from these results, however, that many nontrivial interactions with the cladding modes and resonances with the cladding itself are evident in the confinement loss behaviour of the calculated modes (an observation made for both air-Bragg and Kagomé fibres numerous

times before, as discussed above). The investigation into the novel effects discussed here, such as the anomalous polarisation dependent resonance-like features in the CL spectra, is required before the guidance mechanisms of such fibres (spider-web, air-Bragg and Kagomé alike) can truly be understood in order to influence future structure designs and better understand the guidance mechanisms in their own right.

These results thus indicate that the spider-web design holds much promise as a platform for low-index guidance since it exhibits modal traits very close to both air-Bragg and Kagomé type fibres but via a more simple geometry. Structurally, the spider-web geometry is more flexible for design purposes since the structure places few restrictions, permitting (within fabrication and guidance limits) arbitrary ring, air gap and strut thicknesses, polygonal vertices (hence the numbers of struts) and numbers of rings. Efforts towards fabricating such a structure and the light guidance properties in experiment and theory thereof, are presented in Chapter 5.

2.8 Concluding Remarks

Using a variety of modeling techniques, the guidance mechanisms of idealised air-core all-silica air-Bragg fibres have been presented and discussed. Transfer matrix and finite element methods have been shown to produce more accurate confinement loss calculations for the considered idealised air-Bragg fibre than the previously used asymptotic transfer matrix method (§ 2.4.1). Using semi-analytic techniques, the guidance properties of these waveguides calculated using the aforementioned numerical methods were compared and contrasted to the modal guidance properties of a simple tube and a Bloch mode analysis of the layered cladding (§§ 2.4.1 and 2.4.2).

By examining the bandgap structure of the fibre cladding it has been shown that the Bragg stack exhibits a nontrivial topology of bandgaps (which form the basis of the work of Chapter 3), especially close to the low-index light-line (§ 2.5). It was shown that single-material air-Bragg fibres can access higher order, wider, bandgaps unavailable to conventional Bragg fibres with core refractive indices much lower than the lowest of the cladding indices (§ 2.6). A scheme for exploiting the higher order gaps at a specific wavelength via a global scaling of the fibre geometry was proposed and favorably compared to scaling only the core radius when considering the fundamental bandgap (§ 2.6)—by accessing the second order bandgap closest to the light-line, the idealised all-silica Bragg fibre considered could potentially achieve a minimum confinement loss four orders of magnitude smaller than that attainable by using the fundamental gap. By incorporating these principles into fabricable fibre designs, it is expected that the confinement loss can be reduced to levels where other loss mechanisms become dominant.

Calculations of the modal confinement loss properties of all-silica air-Bragg fibres including the connective cladding struts were also performed (§ 2.7). It was generally observed that the influence of the extra cladding features is predominantly to fracture the CL spectrum by introducing various loss features. Aside from the already known surface-mode anticrossings which introduce fine loss peaks into the CL spectrum of all supported core modes, the present work identified several large anomalous resonance-like loss features in the CL spectra. These novel loss features were present for all structures containing connective cladding struts, regardless of their distribution. Two of the observed resonance-like losses were absent from the CL spectrum of the TE_{01} mode, indicating that the origin of these dominant confinement loss features is polarisation dependent; a predominance of TE field components appears to circumvent the underlying loss mechanisms for these particular features and appears to be the case for all strut-laden structures considered. In the same vein, the TE_{01} mode of all structures was shown to have CL much closer to its strutless equivalent geometry in comparison to the TM_{01} and HE_{11} modes. This sees that the TE_{01} mode is, as for the idealised case (no struts), the lowest loss mode of all structures considered, significantly helped by its invulnerability to two of the anomalous loss features.

The conversion of annular cladding rings to hexagonal rings saw that the modal confinement loss spectra became significantly 'noisier' than their circular counterparts upon the addition of struts (§ 2.7.2). These noisy spectra are very similar to those calculated elsewhere for full Kagomé fibre structures and reveal the close relationship between them. These rapidly fluctuating loss features were superposed upon similar CL curves observed for the circular equivalent structures. These points highlight that the polygonal ring spider-web geometry would guide in a similar fashion to both the Kagomé and air-Bragg structures (and thus potentially share their exotic guidance regimes), thus providing a flexible platform for a novel HC-MOF design—critical for the motivation of Chapter 5.

Given that all considered strut-laden geometries essentially produced CL spectra similar to those of their strutless analogues, the principles of confinement loss reduction via exploitation of higher-order bandgap/resonances would thus follow naturally to them as well, pointing a way towards a better understanding of the design principles required for advancement of air-Bragg, Kagomé or spider-web structure HC-MOFs.

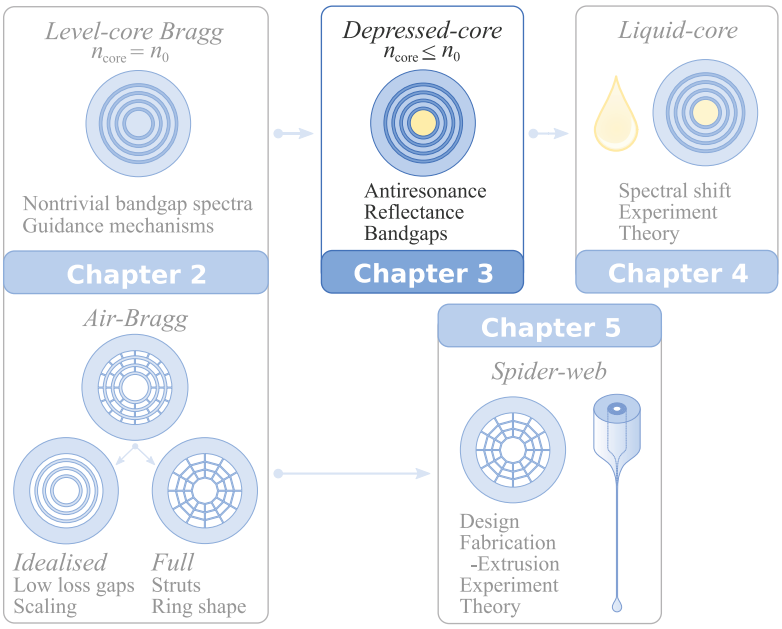
Level-core Bragg
$n_{core} = n_0$
Nontrivial bandgap spectra
Guidance mechanisms
Chapter 2
Depressed-core
$n_{core} \leq n_0$
Antiresonance
Reflectance
Bandgaps
Chapter 3
Liquid-core
Spectral shift
Experiment
Theory
Chapter 4
Air-Bragg
Idealised
Low loss gaps
Scaling
Full
Struts
Ring shape
Chapter 5
Spider-web
Design
Fabrication
-Extrusion
Experiment
Theory